# Simulation and Optimization of Pulsed Chemical Exchange Saturation Transfer for Clinical Application at 3T

By

**Blake Dewey**

**Honors Thesis**

Submitted to the Faculty of the
Department of Physics and Astronomy of Vanderbilt University
in partial fulfillment of the requirements
for
DEPARTMENTAL HONORS
in
PHYSICS

April, 2013
Nashville, TN

Primary Advisor:
Dr. Seth Smith

Committee of Examiners:
Dr. Med Webster
Dr. Richard Dortch
Dr. Manus Donahue

# Abstract

Chemical Exchange Saturation Transfer (CEST) is often overlooked as a method for the investigation of metabolites in vivo due to the time required to obtain a full spectrum. We investigated the feasibility and optimization of a pulsed CEST technique that interleaves an echo planer imaging (EPI) readout with saturation in order to reduce time. In addition, we incorporated a multi-shot EPI sequence that reduces distortions. To achieve this, computer simulations based on the Bloch equations were used to optimize scan parameters while keeping scan time in the clinical timeframe. To analyze the data, a number of Lorentizian fitting algorithms were investigated to evaluate their ability to isolate CEST contrast. By using a 30 ms pulse at 2 $\mu$T, we were able to achieve CEST contrast on the order of 2% and could provide APT maps based on an adapted Lorentzian fitting method. In the process of this fitting, it was also discovered that MTR contrast could also be recovered from the CEST data, allowing for MT and CEST to be acquired at the same time.

# Acknowledgments

Impossible. That is what I would have thought, had someone told me that I would be writing a piece such as this. And it would have been just that without the help of so many along the way. Firstly, I would like to thank my advisor, Dr. Seth Smith, who has, from the beginning, supported me and believed in me. Not to mention that he had to suffer through hours of meetings, discussions and my never-ending questions. It is through his commitment to me that this thesis comes to life. Next, I would like to thank the entire staff at the Vanderbilt University Institute of Imaging Science who have helped me along my way. Firstly, to Dr. Richard Dortch and Dr. Adrienne Dula who have tirelessly worked with me to unravel the mysteries of CEST. And also to David Pennell and Leslie McIntosh, who both spent hours assisting me on the scanner, especially when it was being very difficult. Lastly, I would like to thank my family and friends, who have put up with late nights and ill-tempered mornings when my time for sleep was shorter than I would have liked. To each of these people, this is as much yours as it is mine. Thank you.

# Table of Contents

# List of Figures

vi

# CHAPTER 1
# Introduction

Magnetic Resonance Imaging (MRI) has become the forerunner in medical imaging of soft tissue. One reason for this growth is the ability to control MRI contrast, a hallmark that is unmatched in any other imaging modality. This allows researchers to develop new scanning techniques that produce quicker images and images that contain more specific or sensitive information. This thesis will describe one such technique, termed Chemical Exchange Saturation Transfer (CEST), and the resulting CEST effect that provides molecular contrast on the macroscopic scale.

Before going into the details of CEST theory, a cursory overview of the history and mechanisms behind the CEST effect is necessary. Traditionally, MRI contrast relies on the relaxation properties of $^1$H nuclei in free (or bulk) water, reflecting differences in spin-lattice $(T_1)$ or spin-spin $(T_2)$ interaction between tissues[1]. Due to the short $T_2$ of macromolecules and low concentration, conventional imaging cannot produce contrast that sufficiently reflects macromolecular and protein concentration[2]. Therefore, in order to probe protons associated with species other than water, MR scientists resorted to spectroscopic techniques that were challenging *in vivo*[3]. In 1989, Wolff and Balaban researched the effects of off-resonance (with respect to water) radio frequency (RF) irradiation, and showed that such irradiation could, in fact, attenuate the water signal in the same way that an on-resonance pulse would (although to a lesser degree)[4]. This effect, termed Magnetization Transfer (MT), was the result of the transfer of magnetization information between restricted macromolecules and water within tissue, combined with the properties of the free water. Utilization of this effect provided a method (albeit indirect) to probe non-water protons *in vivo*.

The MT effect is a broad term that encompasses more than one physical phenomenon. In general, MT can refer to any transfer of spin information from one $^1$H nucleus to another neighboring $^1$H nucleus. This transfer can occur through space via two distinct pathways, by either molecular dipole interaction or direct chemical exchange. In molecular dipole exchange, the spin information of one proton influences another spin through space, while direct exchange is the physical interchange of a macromolecular proton with a water proton. In tissue, this interaction takes place between the saturated, restricted solute protons and the free water protons, which we are able to image using standard MRI techniques[5].

MT is an umbrella term, however, and as research progressed, more specific applications of the MT effect began to emerge. In 2000, Ward expanded upon the MT framework by utilizing lower power RF irradiation (on the order of 1-2 $\mu$T compared to greater than 10 $\mu$T utilized in MT) and focusing on a much narrower spectral range (-10 ppm to 10 ppm compared to the range of -100 ppm to 100 ppm often used in MT experiments). This technique allowed for the inspection of direct chemical exchange between mobile protons (e.g., protons that are a part of amide or amine functional groups) and free water contained within tissue and was termed Chemical Exchange Saturation Transfer (CEST), as at low power it was believed that direct chemical exchange dominates. In this study, Ward was investigating the feasibility of an exogenous contrast agent that would produce contrast enhancement after RF irradiation as Gadolinium does in $T_1$ weighted imaging. However, in the process, he opened the door to the existence of endogenous contrasts arising from CEST effects[6]. These include Amide Proton Transfer (APT)[7], myo-inositol CEST (miCEST)[8], glutamate CEST (GluCEST)[9], and creatine CEST (CrCEST)[10], all of these representing a specific metabolite whose exchanging protons are targeted using CEST.

In CEST, we rely on the varying chemical shifts of non-water protons to selectively irradiate pools distinct from the bulk water present in tissue. These distinct protons exist in one of many milieus and communicate with each other through exchange. The selective irradiation is then exchanged with the water resulting in signal attenuation when a measurement is made

on those water protons. The magnitude of the attenuation is a result of the concentration and exchange rate of the exchangeable protons. The CEST effect in imaging, therefore, is the exchange of spin information between two specific pools of protons and a resulting attenuation when selective RF irradiation is applied at the chemical shift of labile protons of interest[5].

One must consider, however, that the attenuation caused by the CEST effect is on the order of 1-5% of the direct saturation of water and therefore is often lost in other competing signals. If one were to investigate the CEST range (-5 to 5 ppm) of a MT spectrum (20 $\mu$T irradiation), there would be no CEST signal discernable, as the direct saturation would encompass the entire range, completely enveloping any CEST effect that may have been present. This is an extreme example, as CEST experiments normally operate on a tenth or less $B_1$ power than MT, but it does illustrate the fact that certain parameters must be optimized to produce maximum CEST contrast. For example, a simple saturation pulse only has two optimization parameters, the duration and amplitude of the pulse. This is also a simplistic example as well, as we find that the pulse must be impractically long in order for the magnetization to reach its steady state, where oscillations fall away and leave a steady value with time. Therefore, we also investigate more complicated examples such as a pulse train that relies on a set of short pulses to achieve saturation and integrate delays to accommodate scanner limitations. This also incorporates more variables to optimize, such as the delay between pulses (controlled by the duty cycle) and the number of pulses in a train. With the pulse train, we must also consider scan time as the amount of time required to play out the pulse train many times is quite intensive. This leads us to the pulsed CEST methods, which interleaves readout gradients with the saturation pulses to save time and improve the efficiency of the approach to steady-state. But even here there are things that act against us. Small pulses by themselves cause smearing of the spectrum among other things. In addition to all of these concerns, each method requires different optimization strategies that must be undertaken in order to produce favorable results.

Finally, it is important to mention that an optimal sequence for APT imaging may not be well optimized for other labile proteins. For example, APT imaging centers on the amide

peak that lies at 3.5 ppm and exchanges with a rate of approximately 30 Hz. As we expect the optimal power to be on the order of the exchange rate, we would expect to need a 0.75 $\mu$T pulse[11]. This is in contrast to miCEST, which resonates at 0.5-1.0 ppm and exchanges at 1 kHz. By the same logic, we would require a pulse that is much stronger (>10 $\mu$T) in order to have optimal contrast. This does not even consider the effect of direct saturation that would greatly affect miCEST, but is less important in APT imaging. With this in mind, if we need a clinically acceptable scan that can isolate more than one exchange regime, significant work must be done to find a middle ground that provides good contrast for each of the metabolites considered.

To undertake these challenges that face CEST imaging, I incorporated computer simulations with *in vivo* scanning of healthy controls and multiple sclerosis patients to determine the optimum configuration that would allow for maximum CEST contrast within the clinical scan time limit of around 15 minutes. By first establishing a range of parameters from simulation, I was able to determine which scans would be feasible and which would provide worthwhile results. Then through experimentation *in vivo* other considerations not present in simulation, such as readout techniques and signal averaging were tested and weighed against the scan time that is required to perform them. Finally, when examining the data from a CEST scan, the CEST effect must be isolated from MT, direct saturation and other competing factors by computer analysis. In order to achieve this, I evaluated a number of Lorentzian fitting algorithms to asses their effectiveness in isolating the APT-CEST effect. After each step was completed, we found a method that would allow the clinical feasibility of CEST imaging with optimized results.

# CHAPTER 2

# Theory

## 2.1 Bloch Equations

The basis of MRI is that the nuclear (in our case $^1$H nuclei) magnetization can be influenced by static and time-varying magnetic fields and through interaction with other nuclei (relaxation). Beginning in 1946, this phenomenon was formalized by Bloch, who described a set of coupled ordinary differential equations (known as the Bloch equations) that capture the change in magnetization due to an applied magnetic field and relaxation[12].

$$
\begin{aligned}
\frac{dM_x(t)}{dt} &= \gamma \left( \mathbf{M}(t) \times \mathbf{B}(t) \right)_x - \frac{M_x(t)}{T_2} \\
\frac{dM_y(t)}{dt} &= \gamma \left( \mathbf{M}(t) \times \mathbf{B}(t) \right)_y - \frac{M_y(t)}{T_2} \\
\frac{dM_z(t)}{dt} &= \gamma \left( \mathbf{M}(t) \times \mathbf{B}(t) \right)_z - \frac{M_z(t) - M_0}{T_1}
\end{aligned}
\tag{2.1}
$$

In Equation 2.1, there are three main parts: the magnetization components (in the $x$, $y$, and $z$ directions) and their associated derivatives (also in $x$, $y$, and $z$), the magnetic field (B(t), composed of a static ($B_0$) and time-varying ($B_1$) term) and the relaxation times ($T_1$ and $T_2$). These interactions allow us to specifically influence the contrast in an MRI image. We can manipulate the time-dependent magnetic field through the use of RF pulses of specific frequencies, powers (or flip angles) and shapes. By specifying which pulses are used and their order, a specific result can be reproducibly generated. Similarly, we can also alter the timing of the acquisition pulse sequence to maximize contrast resulting from the relaxation terms $T_1$ and $T_2$. For example, in a spin echo experiment, which consists of a 90-degree pulse followed

by a delay, then a 180-degree pulse and finally a delay and an echo at the echo time (TE), the TE and repetition time (TR) of this sequence can be altered to produce $T_1$ or $T_2$ contrast. In spin echo, a $T_1$ weighted image is created by setting the TE to be short (less than the value of $T_2$ to minimize any $T_2$ weighting), and the TR to be short (less than the value $T_1$ to maximize $T_1$ weighting)[1]. This is just one example of pulse programming, but any pulse sequence can be simulated based on the Bloch equations.

For a transfer experiment (either CEST or MT), off-resonance (with respect to water) RF irradiation is used to saturate the spins of protons with distinct chemical-shifts. For this specific case, the Bloch equations become a set of time-dependent coupled differential equations, which depend on the frequency ($\Delta\omega$) and amplitude ($\omega_1(\text{t})$) in $\frac{rad}{s}$ of the time-varying magnetic field (in addition to relaxation)[13].

$$\frac{dM_x(t)}{dt} = \Delta\omega M_y(t) - R_2 M_x(t) \qquad (2.2)$$
$$\frac{dM_y(t)}{dt} = \Delta\omega M_x(t) + \omega_1 M_z(t) - R_2 M_y(t)$$
$$\frac{dM_z(t)}{dt} = \omega_1 M_y(t) - (M_z(t) - M_0)R_1$$

If we were measuring the direct saturation of water, this would be sufficient (Figure 2.1a), but the transfer effect requires two pools of exchanging protons, whereas the above equations are valid for one pool of spins.

When spins exist in two different pools and are in exchange with each other (e.g. amide protons and water protons) then the equations need to be modified. It should be pointed out that the main differences between the two pools is the resonant frequency and concentration of each proton moiety. By extending the time-dependent Bloch equations, we can describe the interactions of multiple pools of protons[14]. In the two-pool model, there is one interaction (or exchange) between a bulk (or free) water pool and the solute (or labile protein) pool (Figure 2.1b). In this figure, a plot of the saturation z-spectrum, or z-magnetization as a function of off-resonance frequency of RF irradiation, shows two features. First, the direct saturation of

(a) One-Pool Model



(b) Two-Pool Model



(c) Three-Pool Model
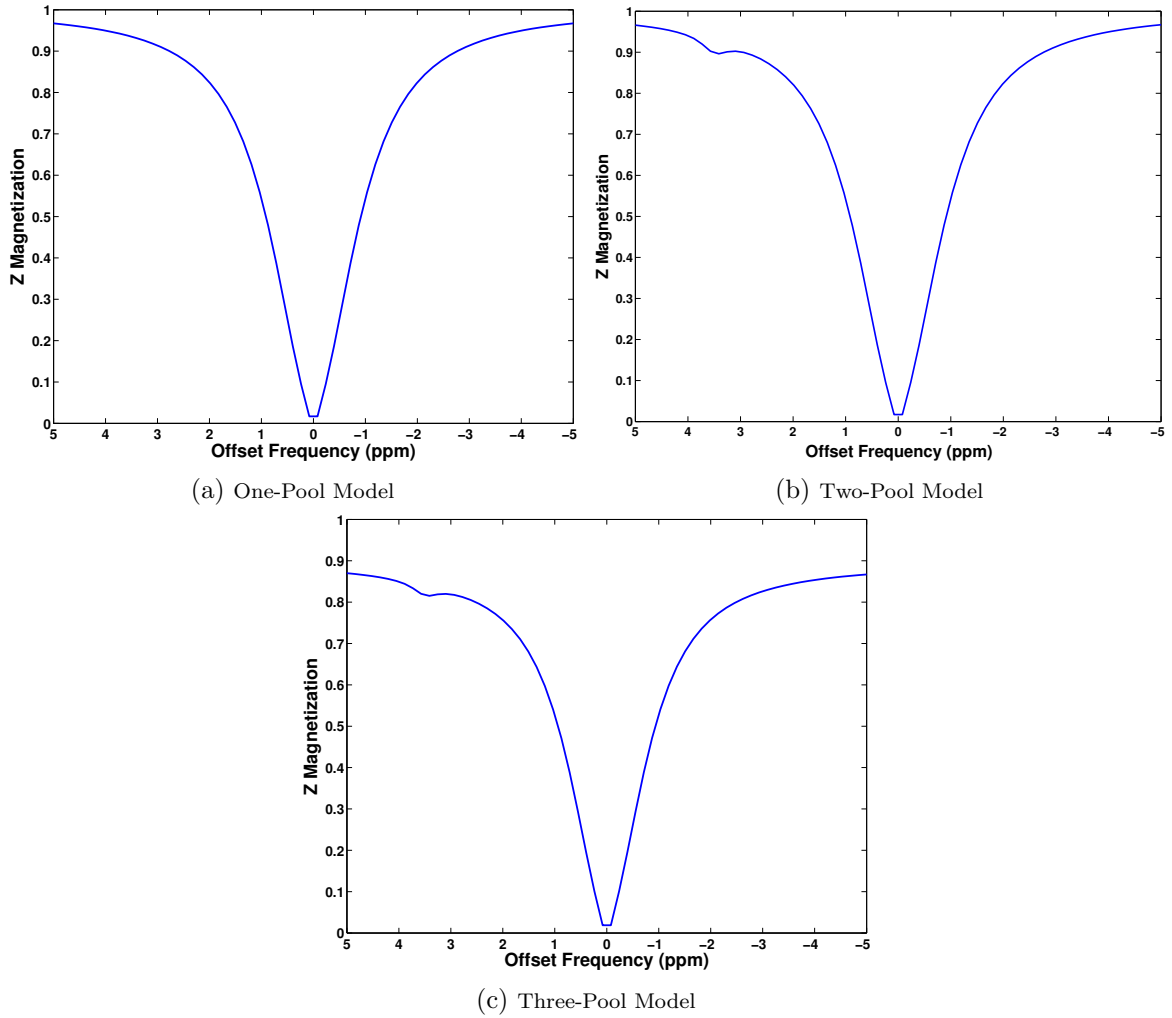
Fig. 2.1: Simulated z-Spectra

the water protons (large signal decrease at 0 ppm) and second the off-resonance proton pool, which is in communication with the water shown as a signal decrease at 3.5 ppm. It should also be pointed out that in a saturation transfer experiment, the water signal is observed, so the signal decrease at 3.5 ppm is a direct result of exchange rather than a signal obtained directly from the protons at 3.5 ppm. Therefore, a saturation transfer experiment is an indirect measurement of the communication between the two pools.

Mathematically, we must extend our Bloch Equations to include the x, y and z components of the second pool of protons (pool b), the forward and backward exchange between the pools ($k_{ab}$, $k_{ba}$), the chemical shift of the pools ($\delta\omega_a$, $\delta\omega_b$), the relative number of the protons in each pool ($M_{0a}$ and $M_{0b}$) and the relaxation rates of each pool ($R_{1a,b}$, $R_{2a,b}$). We must also

define $\Delta\omega_a$ and $\Delta\omega_b$, which includes the RF irradiation frequency ($\Delta\omega$) from Equation 2.2[14].

$$\frac{dM_x^a}{dt} = \Delta\omega_a M_y^a(t) - R_2^a M_x^a(t) - k_{ab} M_x^a(t) + k_{ba} M_x^b(t)$$

$$\frac{dM_x^b}{dt} = \Delta\omega_b M_y^b(t) - R_2^b M_x^b(t) - k_{ba} M_x^b(t) + k_{ab} M_x^a(t)$$

$$\frac{dM_y^a}{dt} = -\Delta\omega_a M_x^a(t) - R_2^a M_y^a(t) - k_{ab} M_y^a(t) + k_{ba} M_y^b(t) + \omega_1 M_z^a(t)$$

$$\frac{dM_y^b}{dt} = -\Delta\omega_b M_x^b(t) - R_2^b M_y^b(t) - k_{ba} M_y^b(t) + k_{ab} M_y^a(t) + \omega_1 M_z^b(t)$$

$$\frac{dM_z^a}{dt} = -\omega_1 M_y^a(t) - R_1^a \left[ M_z^a - M_0^a \right] - k_{ab} M_z^a(t) + k_{ba} M_z^b(t)$$

$$\frac{dM_z^b}{dt} = -\omega_1 M_y^b(t) - R_1^b \left[ M_z^b - M_0^b \right] - k_{ba} M_z^b(t) + k_{ab} M_z^a(t) \tag{2.3}$$

From these coupled equations we can see the influence of the solute pool (Pool A) on the bulk water (Pool B); this is the transfer effect as described mathematically. These equations can be applied to either MT (we have to modify the MT equations to reflect the MT super-Lorentzian lineshape) or CEST pulse sequences, as they are fundamentally the same phenomenon, and only distinguished by the values chosen for each of the parameters.

There are limitations, however, to the two-pool model. We know in tissue that many exchange effects compete, providing a signal that is an intricate convolution of interacting signals[15]. Most commonly, these effects are simplified into bulk water and exchanging protons (ie. MT or CEST in the two-pool model). This means that, in this simple limit, we can only focus on the effect of one target solute (ie. Amide protons in APT), even though, regardless of model choice, our MRI signal will always reflect the full range of interactions. Therefore, to more robustly characterize the effect *in-vivo*, there is a press to include more intricate models. The first iteration is a three-pool model (Equation 2.4) that combines the bulk water (direct saturation), the macromolecular MT effect, and the specific exchanging proton target for CEST[15]. While the details of this model are beyond the scope of this thesis, the key feature is that a three-pool z-spectrum shows a global base-line offset from 1 (due to the macromolecular contributions), direct water saturation at 0 ppm (due to the water contributions), and a CEST

effect (due to the CEST contribution) at 3.5 ppm. A plot showing the resulting z-spectrum of each model is shown in Figure 2.1c. By assuming this model and through careful analysis, the CEST effect can be extracted and analyzed without the competing influence of MT effects.

$$\frac{dM_x^a}{dt} = \Delta\omega_a M_y^a(t) - R_2^a M_x^a(t) - k_{ab} M_x^a(t) + k_{ba} M_x^b(t)$$

$$\frac{dM_x^b}{dt} = \Delta\omega_b M_y^b(t) - R_2^b M_x^b(t) - k_{ba} M_x^b(t) + k_{ab} M_x^a(t)$$

$$\frac{dM_y^a}{dt} = -\Delta\omega_a M_x^a(t) - R_2^a M_y^a(t) - k_{ab} M_y^a(t) + k_{ba} M_y^b(t) + \omega_1 M_z^a(t)$$

$$\frac{dM_y^b}{dt} = -\Delta\omega_b M_x^b(t) - R_2^b M_y^b(t) - k_{ba} M_y^b(t) + k_{ab} M_y^a(t) + \omega_1 M_z^b(t)$$

$$\frac{dM_z^a}{dt} = -\omega_1 M_y^a(t) - R_1^a \left[ M_z^a - M_0^a \right] - k_{ab} M_z^a(t) + k_{ba} M_z^b(t) + k_{ca} M_z^c(t) - k_{ac} M_z^a$$

$$\frac{dM_z^b}{dt} = -\omega_1 M_y^b(t) - R_1^b \left[ M_z^b - M_0^b \right] - k_{ba} M_z^b(t) + k_{ab} M_z^a(t)$$

$$\frac{dM_z^c}{dt} = k_{ac} M_z^a - R_1^c \left[ M_z^c - M_0^c \right] - M_z^c \left[ k_{ca} + W\left( \Delta\omega \right) \right] \tag{2.4}$$

The only difference from the template of the two-pool model (Equation 2.3) is the addition of an absorption line-shape ($W(\Delta\omega)$) to describe the impulsed response of MT pool. This effect arises from dipole-dipole interactions and is distinct from CEST[15].
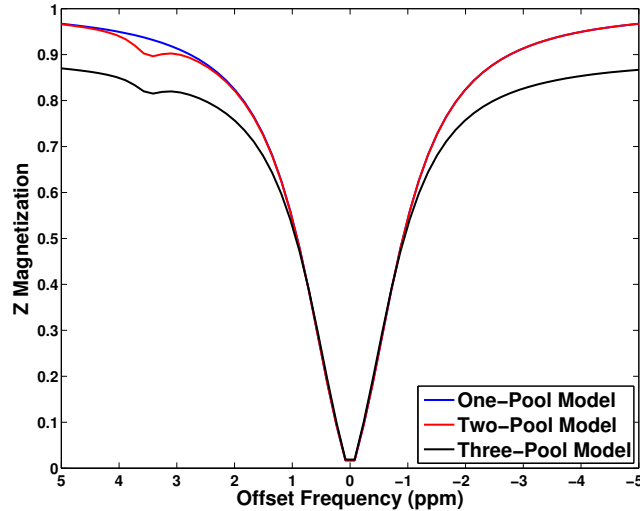


Fig. 2.2: Comparison of Different Exchange Models

One could imagine a system that included many CEST pools to describe every possible

interaction individually. These efforts, however, have not gained much traction as the three-pool model provides a very accurate depiction of the signal and the CEST effect is often analyzed considering one metabolite at a time.

## 2.2   Pulse Sequences

When describing MRI, there are three distinct pieces that comprise every pulse sequence: the preparation, the excitation, and the readout. In the theoretical (CW) limit, the CEST pulse is simply an infinitely long saturation block pulse followed by any type of excitation and readout (Figure 2.3). This, however, is a theoretical limit and cannot be achieved on an actual scanner.
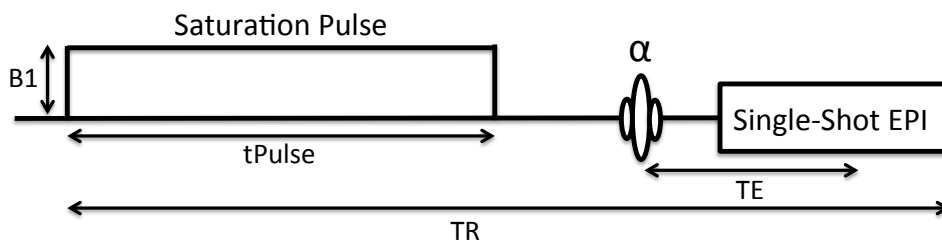


Fig. 2.3: CW Block Pulse

It can be shown that a pulse that is sufficiently long ($\sim$2 seconds), but not infinite, can be used to produce steady state CEST effects. Taking into account scanner limitations, this is still very difficult to achieve *in vivo* and would require significant, advanced programming to avoid fail-safes in the RF amplifiers, not to mention that the scan would be very long compared to most scans in a clinical environment. To overcome the scanner limitations, a pulse train is introduced to replace the single long pulse. By adding delays between multiple, smaller pulses, the amplifier duty cycle is lessened and the scans become more feasible (Figure 2.4), but does not reduce the scan time significantly.

Pulse train CEST introduces another variable into the models, the duty cycle, which is a measure of how much of the repetition time (TR) actually contains a saturation pulse. Since $T_1$ relaxation occurs during the delays between pulses, this affects the overall magnetization at
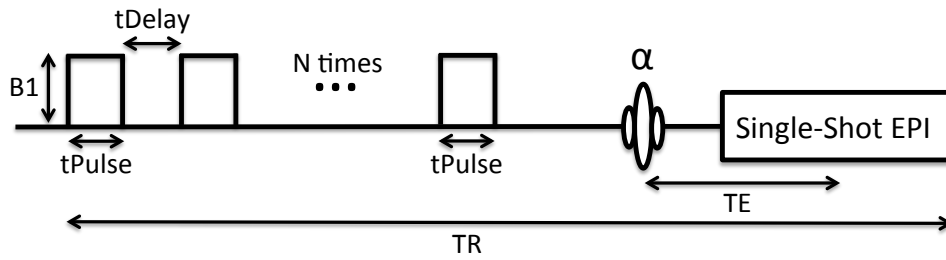
Fig. 2.4: Block Pulse Train

the conclusion of the pulse train and thus affects the observed CEST effect. Therefore, other parameters such as pulse duration and amplitude must be altered to counteract the effect of the delays. Pulse train CEST allows for sufficient saturation within scanner requirements, but still results in long scan times. This is because the same (if not more) saturation time is required to saturate the target protons before performing the excitation and readout. To minimize scan time, a pulsed CEST approach can be used. Instead of performing a set of saturation pulses, then performing excitation and readout, a pulsed scan allows for the interleaving of acquisition (excitation and readout) pulses with the saturation pulse (Figure 2.5)[16]. This
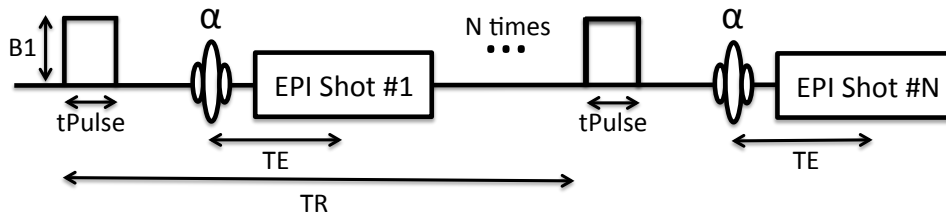


Fig. 2.5: Block Pulsed Sequence

allows for pieces of k-space to be acquired after each pulse, drastically reducing TR and thus scan time. One caveat of this method is that the protons have not reached their steady state before many of the readouts have already occurred. We can address this using the properties of k-space. If we collect data starting on the edges of k-space and make our way to the center, the center of k-space is collected after many saturation pulses, when the saturation is at steady state. Since the contrast in MRI is contained in the center of k-space, this means that, if timed appropriately, our CEST contrast is obtained when our saturation is in steady state[17].

Due to the fact that the signal for a pulsed CEST sequence is dependent on the approach

11

to steady state in relation to the k-space trajectory, it is beneficial to also discuss readout techniques. For our purposes, we consider multi-shot echo planar imaging (EPI) readout schemes as a balance between resolution and speed. Thus, an EPI shot (i.e. a readout of a few lines of k-space) is played out after each saturation pulse and the EPI factor determines the number of pulses (and thus time to the center of k-space).

$$t_{k_0} = \frac{\#ofpixels_\text{phase encode}}{2} \div SENSE_\text{phase encode} \times t_\text{pulse} \qquad (2.5)$$

Using this equation and our three-pool model, we can estimate whether our protons are in steady-state by the time that $k_0$ is reached. It is possible that the center of k-space is reached before the steady-state is achieved, presenting a problem. To overcome this, a 3D acquisition can be employed and thus we can lengthen the time to the center of k-space considerably, as we would have to traverse a 3D volume of k-space rather than the 2D section that is traversed in a traditional multi-slice technique. Choosing to sample k-space from the outside in (from high to low frequencies), regardless of image dimensions, the time to $k_0$ is increased according to number of 3D phase encodes required. Combining these principles, it is possible to develop a pulse sequence that acquires the contrast from a CEST acquisition in steady-state, while minimizing the scan time.

Typical CEST acquisitions assume a block pulse as diagrammed in the above figure, but for pulsed CEST, this is not the most efficient method of saturation. While an infinitely long block pulse would create an ideal signal, the shortening of the pulse from infinity causes k-space artifacts, as the Fourier Transform is no longer infinitely sharp, and causes ringing due to the lobes of the sinc function[17]. For this reason, a number of time-varying amplitude pulses are implemented in MRI scans. These pulses are shaped according to specific Fourier Transform pairs in order to minimize artifacts. Figure 2.6 shows an alternate set of pulse sequences that utilize a sinc-gauss function instead of the traditional block.

(a) Sinc-Gauss Pulse Train
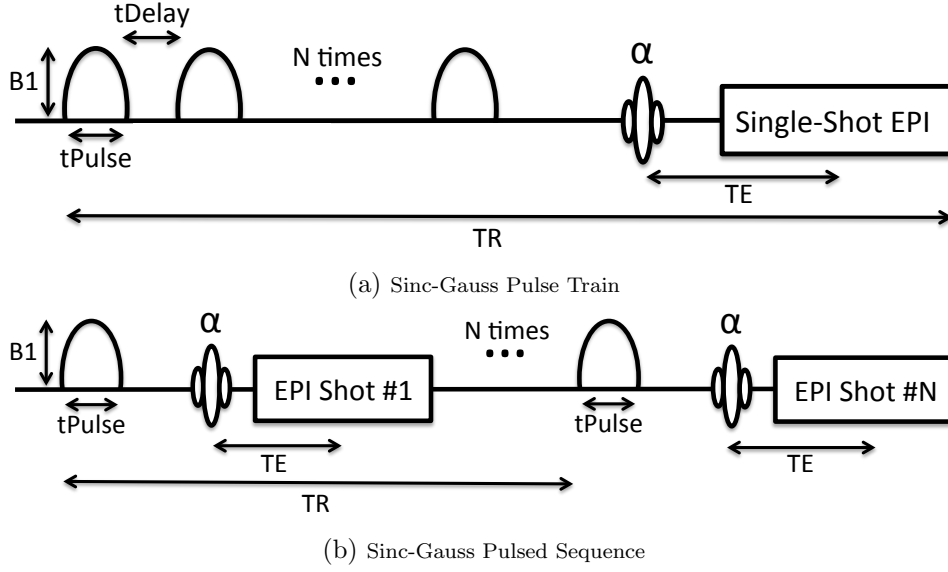


(b) Sinc-Gauss Pulsed Sequence

Fig. 2.6: Pulse Sequences Using Sinc-Gause Shaped Pulses

## 2.3  Simulation

Studying the CEST effect combined with the choice of imaging method presents an optimization problem. In the models above, the assumption for CEST contrast is that the irradiated protons are in steady state. But as stated above, our choice of imaging sequence can influence this. Therefore, we need to simulate the impact of each saturation method on the overall desired contrast. In order to determine optimal RF irradiation values for a given sequence, we first simulate theoretical saturation according to the Bloch equations. For the unmodified Bloch equations for RF saturation (Equation 2.2), Mulkern-Williams[13] devised a solution, which derives the steady state and time dependent magnetization due to a constant and shaped RF pulses (Equation 2.6).

$$M_x(t) = M_x^{ss} + M_x^1 e^{\alpha_1 t} + M_x^2 e^{\alpha_2 t} + M_x^3 e^{\alpha_3 t}$$

$$M_y(t) = M_y^{ss} + M_y^1 e^{\alpha_1 t} + M_y^2 e^{\alpha_2 t} + M_y^3 e^{\alpha_3 t}$$

$$M_z(t) = M_z^{ss} + M_z^1 e^{\alpha_1 t} + M_z^2 e^{\alpha_2 t} + M_z^3 e^{\alpha_3 t} \tag{2.6}$$

This allows us to simulate magnetization profiles (signal vs. time) to determine the

approach to steady state. In addition, by altering the offset frequency ($\Delta\omega$) and taking the final value of a magnetization profile, simulated z-spectra of a direct saturation experiment (ie. without MT or CEST influence) as a function of offset frequency can be produced (Figure 2.1a). This z-spectrum, is the voxel-specific result of a CEST or MT experiment. Due to the lack of analytical solutions to modified versions of the Bloch equations (two- or three-pool models), it is also important to note that there is a valid numerical solution to the Bloch equations that provides accurate estimations of magnetization with minimal computation[14]. This method relies on the matrix solution to a set of differentials.

$$
\begin{aligned}
\frac{d\mathbf{M}}{dt} &= \mathbf{A} \cdot \mathbf{M}, \text{ where} \\
\mathbf{M} &= \left[ M_x(t) \; M_y(t) \; M_z(t) \; 1 \right]^T, \text{ and} \\
\mathbf{A} &= \begin{bmatrix} -R_2 & \Delta\omega & 0 & 0 \\ -\Delta\omega & -R_2 & \omega_1 & 0 \\ 0 & -\omega_1 & -R_1 & R_1 M_0 \\ 0 & 0 & 0 & 0 \end{bmatrix}
\end{aligned}
\tag{2.7}
$$

By creating an appropriate matrix $\mathbf{A}$ (as above), we can provide a valid solution to M(t) given $\mathbf{A}$ through the use of the matrix exponential (Equation 2.8).

$$
\mathbf{M}(t) = e^{\mathbf{A}t}\mathbf{M}(0), \tag{2.8}
$$

$$
e^{\mathbf{A}t} = \mathbf{T}e^{\mathbf{D}t}\mathbf{T}^{-1} = \mathbf{T}diag\left[ e^{\lambda_1 t}, e^{\lambda_2 t}, e^{\lambda_3 t}, e^{\lambda_4 t} \right] \mathbf{T}^{-1} \tag{2.9}
$$

Where $\mathbf{T}$ is the matrix of eigenvectors and $\mathbf{D}$ is a diagonal matrix of the eigenvalues. This matrix exponential is solved cheaply by determining the eigenvalues and eigenvectors for $\mathbf{A}$ and using Equation 2.9. This solution also has the unique property of evolving through multiplication, allowing the multiplication of multiple matrix exponentials together to represent the effect of multiple pulses (or pulse fragments, if estimating a time-varying amplitude). This provides the basis for a simple algorithm that can determine the magnetization profile or final

z-Spectrum of a pulse sequence.

From this base, the modified Bloch equations can be simulated in the same way by simply modifying the A matrix from the previous solution (Equation 2.10)[14].

$$\mathbf{A} = \begin{bmatrix} -\left(R_2^a + k_{ab}\right) & k_{ba} & \Delta\omega_a & 0 & 0 & 0 & 0 \\ k_{ab} & -\left(R_2^b + k_{ba}\right) & 0 & \Delta\omega_b & 0 & 0 & 0 \\ -\Delta\omega_a & 0 & -\left(R_2^a + k_{ab}\right) & k_{ba} & \omega_1 & 0 & 0 \\ 0 & -\Delta\omega_b & k_{ab} & -\left(R_2^b + k_{ba}\right) & 0 & \omega_1 & 0 \\ 0 & 0 & -\omega_1 & 0 & -\left(R_1^a + k_{ab}\right) & k_{ba} & R_1^a M_0^a \\ 0 & 0 & 0 & -\omega_1 & k_{ab} & -\left(R_1^b + k_{ba}\right) & R_1^b M_0^b \\ 0 & 0 & 0 & 0 & 0 & 0 & 0 \end{bmatrix} \quad (2.10)$$

This allows for the consideration of two-pools in the simulation (bulk water and solute) and is capable of simulating the CEST effect with the proper selection of $R_1$, $R_2$, exchange and $\Delta\omega$ values (Figure 2.1b).

Even with this two-pool model, we still see idealized results. For example, *in vivo* data does not have a maximum at 1, as some of these examples have. In addition, they also tend to be asymmetric, while the previous simulations produce a symmetric line shape. The reason for these differences is the confounding effect of MT, which is asymmetric in comparison to the water peak and consists of a very wide ($\sim$50 ppm), shallow (10-20% of the water peak) line shape. In order to account for this difference in the simulations, we introduce another magnetization pool that will account for the semi-solid (MT type) protons. In order to do this, the A matrix from Equation 2.9 must be modified to include the z-magnetization of the semi-solid pool (Equation 2.11)[15].

$$\mathbf{A} = \begin{bmatrix} -\left(R_2^a + k_{ab}\right) & k_{ba} & \Delta\omega_a & 0 & 0 & 0 & 0 & 0 \\ k_{ab} & -\left(R_2^b + k_{ba}\right) & 0 & \Delta\omega_b & 0 & 0 & 0 & 0 \\ -\Delta\omega_a & 0 & -\left(R_2^a + k_{ab}\right) & k_{ba} & \omega_1 & 0 & 0 & 0 \\ 0 & -\Delta\omega_b & k_{ab} & -\left(R_2^b + k_{ba}\right) & 0 & \omega_1 & 0 & 0 \\ 0 & 0 & -\omega_1 & 0 & -\left(R_1^a + k_{ab} + k_{ac}\right) & k_{ba} & k_{ca} & R_1^a M_0^a \\ 0 & 0 & 0 & -\omega_1 & k_{ab} & -\left(R_1^b + k_{ba}\right) & 0 & R_1^b M_0^b \\ 0 & 0 & 0 & 0 & k_{ac} & 0 & -\left(R_1^c + k_{ca} + W\left(\Delta\omega\right)\right) & R_1^c M_0^c \\ 0 & 0 & 0 & 0 & 0 & 0 & 0 & 0 \end{bmatrix} \quad (2.11)$$

Notice that an extra term W term is introduced to alter the $R_1$ contribution of the semisolid pool. This term is included to take into account the absorption lineshape of the MT pool, which varies with the frequency offset. It has been determined that this profile depends on $T_2$ and follows a super-Lorentzian lineshape. Therefore, this super-Lorentzian can be calculated using macromolecular $T_2$ and inserted into the **A** matrix to account for this effect. As the simulation can now account for MT, there is a much better correlation to what one might expect from *in vivo* data (Figure 2.2).

Now that the simulations can reasonably predict *in vivo* results, the pulse parameters can be studied in order to produce optimal CEST contrast. By fixing the physical parameters of the tissues ($T_1$, $T_2$, $k_{ab}$, $k_{ba}$ concentration, chemical shift) to literature values, the remaining variables can be modified to simulate different pulse sequences. For each set of pulse parameters, a z-spectrum can be simulated and the CEST effect can be measured by finding the peak height at the metabolite's chemical shift (eg. 3.5ppm for APT). The CEST contrast is then compared between trials by using a 3D plot (Figure 2.7).
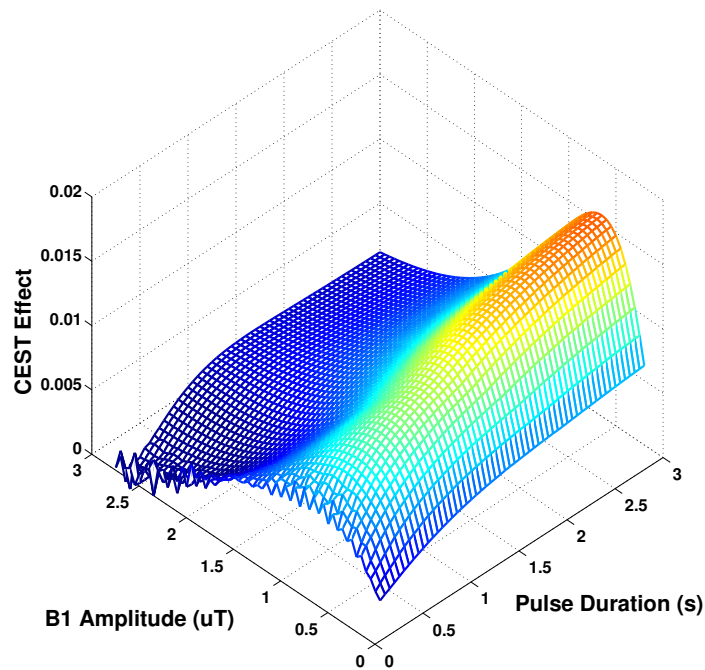


Fig. 2.7: Sample 3D Plot Comparing CEST Effect to Pulse Amplitude and Pulse Duration

Each pulse type must be handled differently in order to model the scanning environment

accurately. For a continuous wave pulse, only the pulse duration and amplitude can vary and the number of pulses is set to 1. It is also important to remember the scanner limits when using a continuous wave pulse, as an infinitely long block pulse would allow for maximum contrast; however, this is infeasible in reality.

In the pulse train scenario, the pulse duration, pulse amplitude, number of pulses and the duty cycle (delay between pulses) can all be varied, leaving a great deal of room for experimentation. However, just as with the continuous wave pulse, there are practical limitations to take into account. For example, the number of pulses must be kept at a reasonable level in order to keep the scan time in the clinical order ($\sim$7-15 minutes). This also puts a great deal of trade-off in terms of the pulse duration, as shorter pulses would allow more pulses in a given period. However, one must consider the bandwidth of the pulse as well, as the shorter a pulse gets, the larger its bandwidth is, causing a loss in sensitivity in the frequency of the pulse. This is a very serious concern for CEST experiments as they rely heavily on frequency selectivity. In addition, the pulse train scenario also must be restricted in its maximum duty cycle due to power deposition and amplifier limitations on the scanner.

Lastly, in the pulsed approach, the pulse duration, pulse amplitude, TR, and the time to the center of k-space ($k_0$) can all be varied, but not all are independent in reality. The pulse duration and pulse amplitude are both independent variables, but the TR and time to $k_0$ are both controlled by the scanner (and other image parameters). The TR is calculated by the scanner in this scenario to account for maximum SAR according to various models. This depends on the pulse duration and amplitude and can be retrieved from the scanner (Appendix A). The time to the center of k-space, however, depends on the TR, image dimensions, SENSE factor (amount of k-space captured), and EPI factor (number of lines of k-space collected per pulse) and can be calculated using Equation 2.5. By optimizing pulse parameters for each pulse type, the time on the scanner is drastically diminished as the simulation gives a starting point for the final optimization.

# CHAPTER 3

# Method Overview

## 3.1   Computer Simulations

All simulations were carried out utilizing the scripting environment in MATLAB 2012b (Mathworks, Natick, Massachusetts) on an Apple iMac (3.0 GHz, dual core CPU). The simulations were conducted under the assumption of a three-pool model as described in the theory section. Each simulation began with starting parameters that defined the physical tissue. Each parameter ($T_1$, $T_2$, $k_{ex}$, concentration etc.) was prescribed according to literature values for the three pools of interest (bulk water, MT and solute). Note that $k_{ex}$ is the exchange between the two pools and can be related to $k_{ab}$ and $k_{ba}$ through a first order mass law. These values are compiled in Table 3.1. With the physical system established, the pulse parameters (pulse duration, amplitude, frequency and delay) were defined. This is where each simulation differed. The purpose of these simulations was to determine the optimal combination of pulse sequence variations to achieve the maximum CEST contrast at 3.5 ppm and reflective of amide proton transfer (APT).

| $^1$H Pool | $T_1$ (ms) | $T_2$ (ms) | $k_{ex}$(Hz) | Relative Conc. |
|---|---|---|---|---|
| Bulk Water | $1290^{17}$ | $64^{27}$ | – | 1 |
| MT (Semisolid) | $1290^3$ | $0.01^{47}$ | $30^{47}$ | $0.1^{47}$ |
| Solute (APT) | $770^{89}$ | $33^{89}$ | $10\text{-}30^5$ | $0.001$ $^{56}$ |
| Solute (Amine) | $770^{89}$ | $33^{89}$ | $20\text{-}1200^5$ | $0.001^{5\ 6}$ |

Table 3.1: Tissue Constants

The first simulation created the magnetization profile (evolution of magnetization versus time). This was performed for a specific pulse (at a specific frequency) and analyzed over a specific period of time. This was then repeated for a set of pulse parameters in each of the pulse sequence types (CW, pulse train, and pulsed). In the continuous wave limit, only the effects of the pulse duration and amplitude were tested and two shapes, sinc-gauss and block, were also compared. In the pulse train case, the effects of the pulse duration, amplitude, number of pulses and duty cycle (delay) were all tested. And finally, in the pulsed case, the effects of pulse duration, amplitude and time to $k_0$ were all tested. For each of these simulations, a plot was made of the magnetization over time and the changes between variables were noted. During this experiment, close attention was paid to the time at which the magnetization reached a steady state, as this is where maximum contrast is achieved and further saturation is unnecessary

The next simulation experiment explored the effect of the pulse parameters on the final z-spectrum. To achieve this, a magnetization profile experiment was conducted at the prescribed pulse parameters and the final value was kept. The experiment was then repeated with a range of pulse frequencies (-10 to 10 ppm at 0.1 ppm intervals). This set of final magnetization values creates the z-spectrum[11]. As this is only an extension of the previous experiment, the same

---

[1][18]

[2][19]

[3]Estimated to be similar to that of water

[4][20]

[5][11]

[6]Based on a 100 mM concentration relative to 115M concentration of bulk water

[7]Values averaged between WM and GM

[8][21]

[9]Values extrapolated from 4.7T data

set of variables was used to simulate the effect on the final z-spectrum. In analyzing the spectra in this experiment, special note was taken of the CEST contrast and the effect of MT, which would be vital to creating an optimal pulse sequence.

The final simulation experiment combined variables into 3D results that displayed the CEST effect (as measured by the maximum value of the CEST peak) in terms of the two strongest influences, pulse duration and amplitude. For the CW case, only duration and amplitude were tested. In the pulse train cases, the number of pulses and pulse delay (duty cycle) were also varied creating a number of 3D plots for comparison. For each of these plots, maximum values were weighed against practical constraints to determine an optimal pulse configuration.

## 3.2   *In Vivo* Scan Protocol

All MRI scans were performed on a Philips 3T Achieva MRI Systems (Philips Medical, Best, The Netherlands) using an 8-channel head coil for reception and a 2-channel transmit body coil for excitation and RF irradiation. SAR limitations were observed following FDA guidelines ($< 3$W/kg). All scans were run using a modified software patch developed in-house for the implementation of CEST and MT sequences. All control subjects were taken from a volunteer pool of undergraduate college students (7 Controls, Mean Age 20.3, 5 Female/2 Male), all of whom provided informed consent following the protocols established by an Institutional Review Board. This sequence was also tested in a Multiple Sclerosis (MS) patient (Age 34, Male), diagnosed with relapsing remitting multiple sclerosis (RRMS).

The scan protocol contained 3 main acquisitions: survey and reference scans, anatomical scans, and CEST acquisitions. The first section, survey and reference, contained a $T_1$ tri-planar planning scan that allowed for the geometric planning of further scans, a SENSE reference scan, and a $B_1$ calibration scan to allow for multi-transmit scanning. The second section, anatomical scans, contained a $T_2$-weighted turbo spin echo sequence to give anatomical information and a

$T_1$-weighted MPRAGE sequence to allow for delineation of gray and white matter (and eventual segmentation of these tissues). The final section, CEST scans, contained a $B_0$ and $B_1$ field maps to determine static and transmit field inhomogeneity across the field of view and the experimental CEST scans (which varied depending on the variables being tested). All scans were obtained using a 220x220x100 mm$^3$ field of view with 2x2x5 mm$^3$ resolution (reconstructed to a 256x256 matrix). CEST data was obtained for 63 offset frequencies from -5 to 5 ppm and at one frequency far from the water resonance ($\sim$80000 ppm) for normalization. Each scan was acquired in 3D with a SENSE factor = 2 in the AP phase encode direction. The large number of slices was used to reduce z direction fold-over and to mimic whole-brain clinical settings.

## 3.3    Pulse Sequences

Three types of pulse sequences were employed to elicit CEST effect: continuous wave, pulse train and pulsed. Each of these was obtained by altering the saturation pulse and the readout scheme. For continuous wave, a single pulse of the maximum duration allowed by the scanner was used. This was followed by a single-shot EPI sequence, capturing all of k-space at one time (Figure 2.3). For the pulse train, the pulse duration of the saturation pulse was shortened and the number of pulses was altered to compensate. The duty cycle was then set to the maximum allowed by the scanner. This was also followed by a single-shot turbo field echo (TFE) readout (Figure 2.6a). In the pulsed case, the number of pulses was reduced to one and the EPI sequence was changed to multi-shot. This would allow one, segmented EPI readout to be performed for each saturation pulse. The EPI factor (number of lines of k-space acquired per readout) was altered to change the number of pulses used. By altering the EPI factor, the number of shots (readouts) was altered, as the number of lines of k-space required always remained the same. Therefore, a smaller EPI factor would increase the number of pulses sent before the center of k-space was reached. Each of these sequences was then repeated for each of the prescribed frequencies to produce the entire CEST volume. In each pulse sequence a 19

degree excitation pulse was used to begin readout. To counteract the effects of lipid interactions a binomial (1331) water selective pulse was applied for the readout excitation.

## 3.4    Image Analysis

Each of the scans was reconstructed on the scanner and exported using the Philips proprietary PAR-REC format. First, the $T_1$-weighted anatomical image was segmented (white/gray matter) using the Fuzzy C Means Multispectral algorithm in MIPAV (National Institutes of Health). This was then exported to NIFTI format and imported into Matlab. The segmentation was then separated into three different classes to use during the analysis process, the whole brain, the white matter and the gray matter. After the masks were created, a CEST volume was imported into Matlab using in-house functions, creating a 4D array representing the CEST data. The baseline volume was then extracted and the CEST data normalized by dividing each CEST voxel by the corresponding baseline voxel (Equation 3.1). This value is termed the CEST ratio (CESTR) and represents the magnetization with respect to an equilibrium (beginning) magnetization of 1.

$$CESTR_i = \frac{CEST_i}{S_0} \tag{3.1}$$

Voxel by voxel, the CEST ratio produces a z-spectrum. We then explored methods to appropriately fit these spectra using the solutions to the modified Bloch equations. There are many methods that are presented in literature to fit z-spectra and even more that are possible but yet undocumented. Each of these can be easily implemented by using the `lsqcurvefit` function within the Matlab library. The simplest of these only requires the fitting of one Lorentzian centered at the water peak (Equation 3.2).

$$L = \frac{A\Gamma^2}{\Gamma^2 + 4\left(\Delta\omega - \delta\right)^2} \tag{3.2}$$

This method can accurately fit the center and width of the water peak, but fails to correctly determine the MT effect, which dampens the signal asymmetrically across the entire frequency range (Figure 3.1a)[22]. In a CEST study at 7T, Jones et al. implemented a simple correction



(a) One-Pool Method

(b) Jones Method

(c) "Tacked" Jones Method

(d) Three-Pool Method
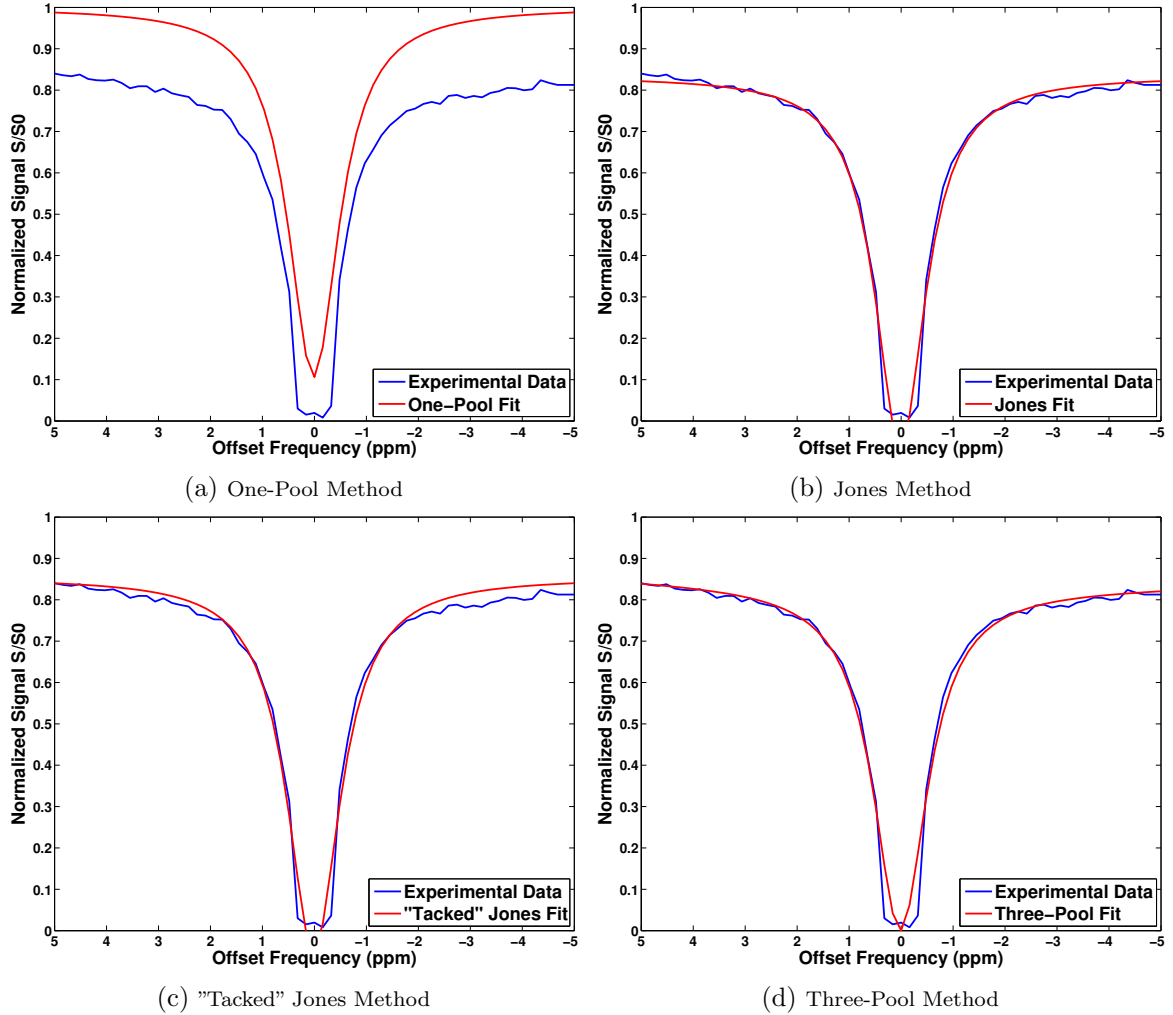
Fig. 3.1: Sample Lorentzian Fits to Experimental Data

to this by adding a constant term, the baseline, b, to the Lorentzian equation, which can be shown to approximate the MT effect (Equation 3.3)[23].

$$L = \frac{A\Gamma^2}{\Gamma^2 + 4\left(\Delta\omega - \delta\right)^2} + b \tag{3.3}$$

This method, however, fails to provide positive values for the CEST residual at frequencies far from the water resonance (Figure 3.1b). By adding yet another constant, the Jones method

can be altered to correct for the depression in the Lorentzian (Equation 3.4).

$$L = \frac{A\Gamma^2}{\Gamma^2 + 4\left(\Delta\omega - \delta\right)^2} + b$$
$$Lorentzian = 1 - L + c \tag{3.4}$$

This method, termed the tacking method, tacks the Lorentzian to the maximum value of the data spectrum and does not assume that the Lorentizan reaches its peak by the end of the z-spectrum (Figure 3.1c).

In addition to a simple one-pool model fit, one can extend the model to include each of the three contributing pools to provide a different fit. This method, recently documented by Zaiss et al., uses the mathematical solution to the modified Bloch equations to model a three-pool system of Lorentzians (Equation 3.5)[24].

$$L_i = \frac{A_i\Gamma_i^2}{\Gamma_i^2 + 4\left(\Delta\omega - \delta_i\right)^2}, where\ i \in \{a, b, c\}$$
$$CTR = \frac{L_b + L_c - 2L_bL_c}{1 - L_bL_c}$$
$$Z\text{-}Spectrum = 1 - \frac{\left(L_a\left(1 - CTR\right) + CTR\left(1 - L_a\right)\right)}{\left(1 - CTR \times L_a\right)} \tag{3.5}$$

Each of these three Lorentizans can be fit at once to provide a comprehensive solution that accurately models the CEST effect. By fitting the three-pools, the solute pool can be separated leaving only the MT and bulk water pools (Equation ]3.6). This allows for a residual that subtracts the data from the remaining two pools, theoretically leaving only the solute pool remaining (plus whatever fitting error may be present).

$$L_i = \frac{A_i\Gamma_i^2}{\Gamma_i^2 + 4\left(\Delta\omega - \delta_i\right)^2}, where\ i \in \{a, b, c\}$$
$$Z\text{-}Spectrum = 1 - \frac{\left(L_a\left(1 - L_b\right) + L_b\left(1 - L_a\right)\right)}{\left(1 - L_bL_a\right)} \tag{3.6}$$

Each of these four methods provides different fits and thus different results. To analyze the

CEST ratio, each voxel was fit to each of the models listed above. In order to save computing time, 5 slices were chosen at the center of the brain as a representative sample. After each fit is complete, the center of the water fit was determined and the data was shifted along the frequency axis to shift the center to zero in each voxel. This has the effect of eliminating any $B_0$ inhomogeneity that may be present in the data (Figure 6.3a). A map was made of these shifts and compared to the acquired $B_0$ field map to determine that accuracy of the shifts (Figure 6.3b and 6.3c). After the data was shifted, the Lorentzian was adjusted accordingly and a residual was calculated that quantified the difference from the fit to the acquired data at each offset. The CEST effect was then calculated by integrating under the residual for an area centered at at the point closest to the solute resonance frequency. This data was then collected and displayed as a residual map for visual analysis.

# CHAPTER 4

# Computer Simulation

## 4.1 Magnetization Profiles

The first simulations were those creating magnetization profiles from specific pulse parameters. First, we considered the continuous wave saturation method. CW was simulated by implementing a single 3000 ms block pulse at 3.5 ppm relative to water and plotting the evolution of $M_z$ over time (Figure 4.1).
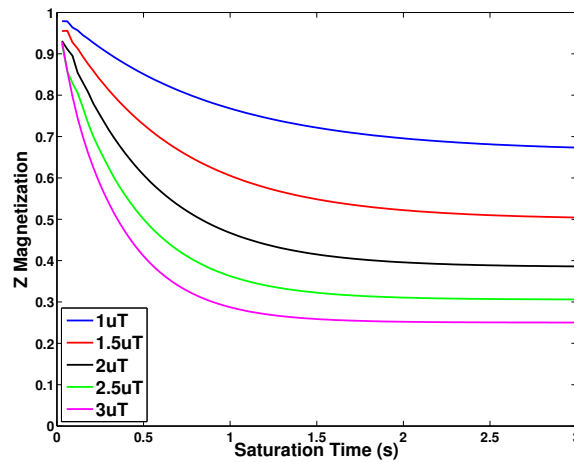


Fig. 4.1: Effect of $B_1$ on the Magnetization Profile for a CW Block Pulse

Figure 4.1 shows the effect of both pulse duration and $B_1$ amplitude simultaneously. The z magnetization is saturated (attenuated) to a lower value with increasing $B_1$ amplitude. For any one $B_1$, the effect of the pulse duration is that as the pulse was lengthened the $M_z$ approaches a steady state saturation level, which it approaches asymptotically. This is the expected result as a long pulse duration results in simplified solutions to the Bloch equations. For these simulations the steady state occurs between 1650 ms and 1950 ms, with increasing

$B_1$ amplitude. It should be pointed out that due to amplifier restrictions, greater than 500 ms pulses cannot be generated, and no significant saturation can be achieved in this manner. This figure also shows the effect of decreased spacing between the individual $B_1$ amplitude plots with increasing $B_1$. This can be interpreted as an asymptotically approaching maximal saturation.

In addition the effects of $B_1$ amplitude, the effect of solute offset frequency was tested while holding a constant $B_1$ amplitude of $1\mu$T (Figure 4.2).



(a) Far From Bulk Water
Resonance ($\geq$2ppm)

(b) Near Bulk Water
Resonance ($\leq$2.5ppm)
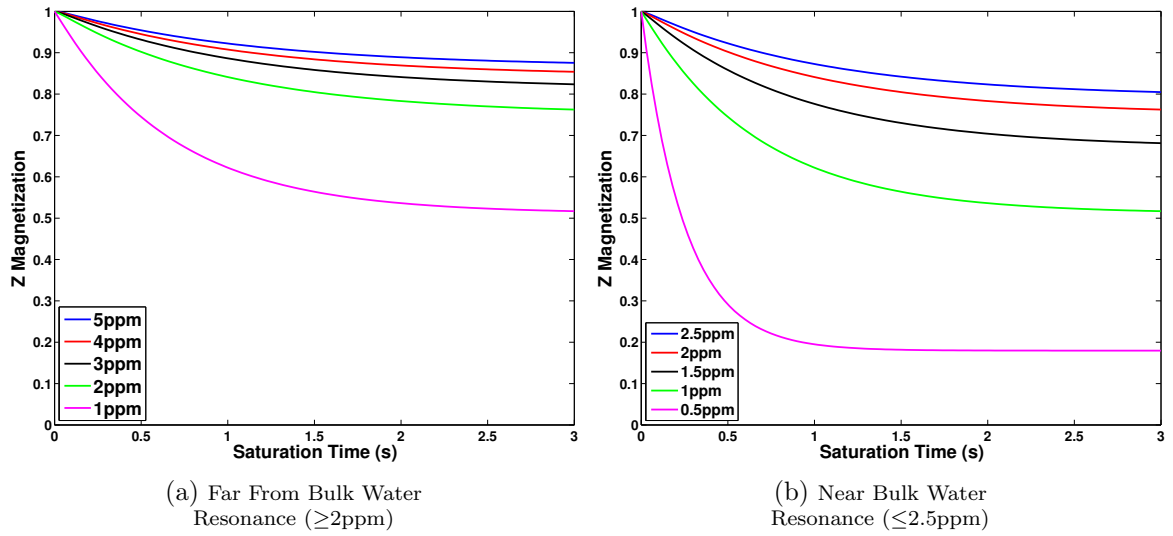
Fig. 4.2: Effect of Offset Frequency on the Magnetization Profile for a CW Block Pulse

In Figure 4.2, it is clear that the decreasing offset frequency (moving closer to the water resonance frequency) depresses the z magnetization. This confirms the fact that the signal is attenuated first by the asymmetric MT effect (Figure 4.2a) at frequencies greater than $\sim$2 ppm, then by the direct water saturation at values inside 2 ppm (Figure 4.2b). This builds the basis for the z-spectrum analysis that will be conducted later, as the z spectrum is merely a collection of the final z magnetization values from a single pulse power and for every frequency sampled.

Next, we show results from a pulse train simulation. This was implemented by 40 30 ms pulses with short delays in between (a 50% duty cycle) and performed simulations where the pulse was either a block pulse or a sinc-gauss shaped pulse (Figure 4.3). The first experiment conducted compared the effects of different $B_1$ amplitudes on the magnetization profile (Figure
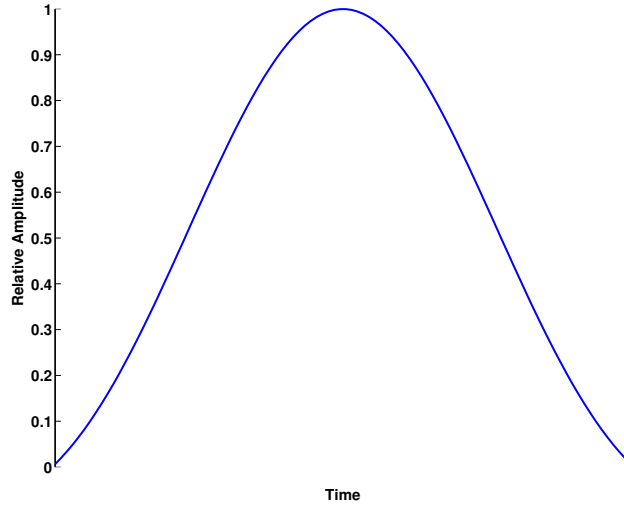
Fig. 4.3: Sinc-Gause Pulse

4.4). (Figure 4.4) shows the effects of different $B_1$ amplitudes on the magnetization profile for a



(a) Block Pulse



(b) Shaped Sinc-Gauss Pulse
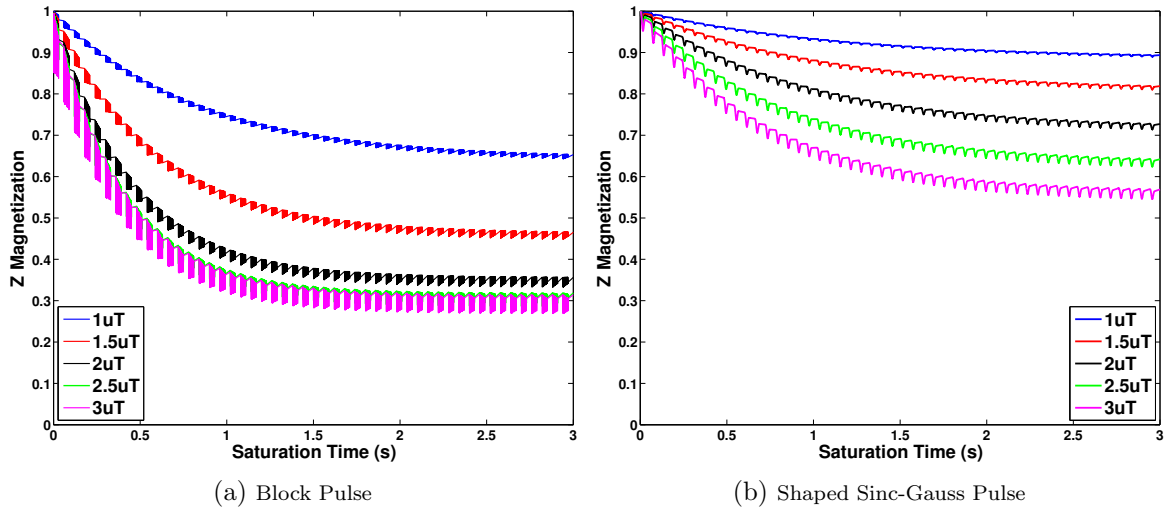
Fig. 4.4: Effect of $B_1$ on the Magnetization Profile for a Pulse Train

pulse train comprised of block pulses and shaped pulses. Note these simulations do not produce a smooth saturation to steady-state, as the CW does, because of the relaxation that happens between each pulse, and the incomplete saturation that occurs after each pulse. Nevertheless, a pulse train can generate a dynamic steady-state saturation.

We can see in both of the plots in Figure 4.4 that the effect of increasing $B_1$ amplitude mimics the trends for CW, but the approach is significantly different. Here we can also see the effect of an increased number of pulses. As the length of the pulse train increase (i.e.

28

the number of pulses increases), the magnetization reaches its steady state, which still occurs between 1650 and 1950 ms. Note that these values are unique for the solute, relaxation and field strength used in our simulation and will be different for different field strengths, etc. The transition to steady state is slightly different for shaped compared to block pulses, and in fact, a shaped pulse, pulse train (Figure 4.4b) shows a marked reduction in the oscillations versus block pulses (Figure 4.4a) during the transient approach to steady state. In addition to the $B_1$ amplitude, the individual pulse duration was evaluated. To simulate this we began with a set of 150 20 ms pulses at a $B_1$ amplitude of $1\mu$T and a duty cycle of 50% and increased the pulse duration in 10 ms increments, while adjusting the number of pulses to keep the total pulse train length the same (Figure 4.5). From Figure 4.5 we can see, that many shorter pulses
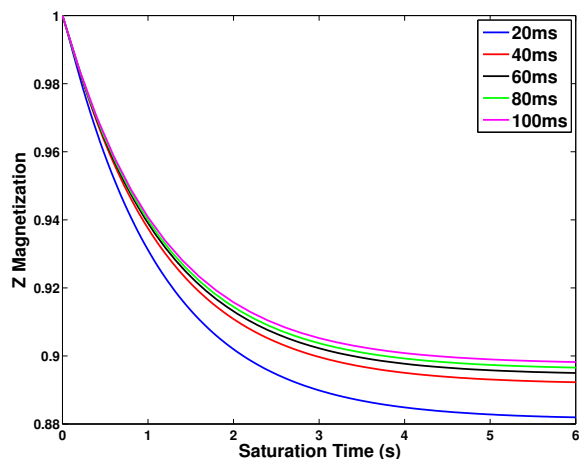


Fig. 4.5: Effect of Pulse Duration on the Magnetization Profile for a Sinc-Gauss Pulse Train

produce a greater saturation effect at 3.5 ppm, compared to longer, fewer pulses. In essence, we are moving closer to the limit of an infinite number of infinitesimally short pulses, which in the high duty cycle limit, is defined as CW. For all pulse train simulations, the duty cycle was kept at 50% to distinguish it from the CW, but also because most scanners can easily perform a 50% duty cycle. However, the impact of the duty cycle was simulated using a pulse train of 30 ms pulses at duty cycles from 50% to 90% in 10% increments. Each pulse train length was 3000 ms and the saturation was played out at 3.5 ppm (Figure 4.6). In Figure 4.6, we can see that increasing the duty cycle increases the magnitude of saturation as an increase in duty cycle results in more saturation time and less relaxation time per TR. For the final
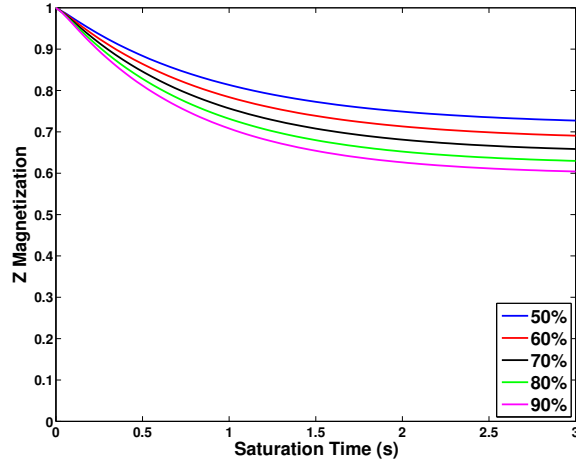
Fig. 4.6: Effect of Duty Cycle on the Magnetization Profile for a Sinc-Gauss Pulse Train

simulations, we examined pulsed CEST. Recall this is one CEST pulse per TR interleaved with a multi-shot readout. In this experiment, a SAR model that is built into the scanner software determines the minimum TR given a particular RF pulse duration and amplitude. This model is detailed in Appendix A. In order to simulate this effect, we chose the shortest TR allowed by the model for each set of RF parameters. In addition, instead of setting a number of pulses (as in the pulse train), the pulsed CEST sequence is related to the time to the center of k-space $(k_0)$ . Using this we can simulate a pulsed sequence by determining the number of pulses necessary by dividing the time to $k_0$, by the TR. Therefore, in order to fully investigate the pulsed CEST technique, we simulated the effects of pulse duration, and pulse amplitude and observed the necessary time to $k_0$ that must be implemented *in vivo* in order to reach steady state magnetization. The magnetization profile as a function of $B_1$ (for a fixed 30 ms sinc-gauss pulse)(Figure 4.7) shows, similarly to each of the other CEST methods, that an increase in $B_1$ amplitude results in greater saturation. In contrast to the pulse train example, however, increased pulse duration, at a constant $B_1$ amplitude (1 $\mu$T for this simulation) will also increase saturation (Figure 4.8).

By examining the magnetization profiles, we can see that our simulations match what we would expect from background on the CEST effect. Therefore, we feel comfortable in any prediction that is based on these values (z-spectra or 3D plots).
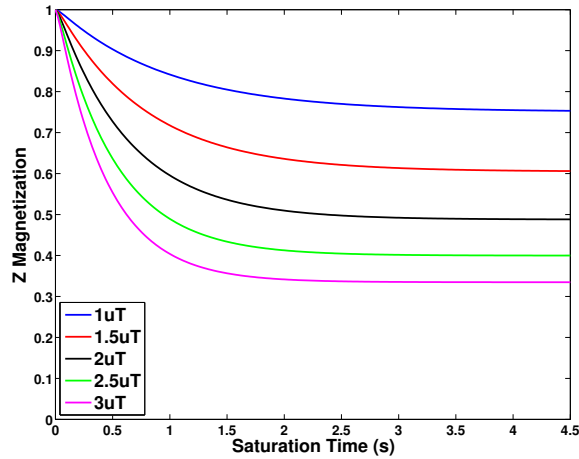
Fig. 4.7: Effect of $B_1$ Amplitude on the Magnetization Profile for a Sinc-Gauss Pulsed Sequence
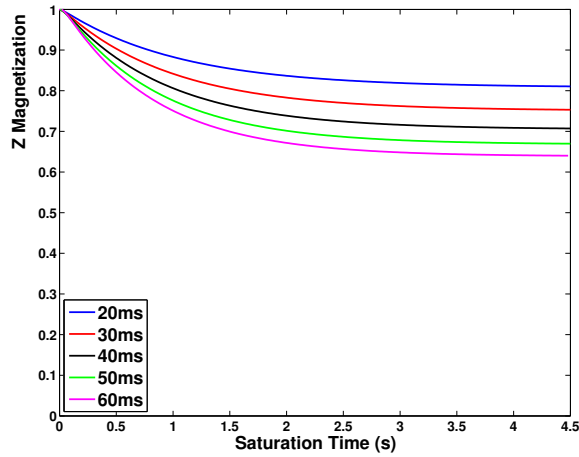


Fig. 4.8: Effect of Pulse Duration on the Magnetization Profile for a Sinc-Gauss Pulsed Sequence

## 4.2   Z-Spectra

From the magnetization profiles, we turn our attention to CEST z-spectra to highlight the impact of pulse sequence design on the observed saturation at the desired CEST resonance frequency. For z-spectra, we simulated spectra of offset frequencies (63 offsets from -5 to 5 ppm relative to water) using the 3 pool model. Beginning with CW, we simulated z-spectra for pulse duration and pulse amplitude effects. To test the effect of pulse duration, the $B_1$ amplitude was held at 1 $\mu$T, while the pulse duration was varied from 50 ms to 1000 ms (Figure 4.9). Figure 4.9 shows that fairly long (>500 ms) pulses are necessary to appreciate the CEST effect at 3.5 ppm. Additionally, for short block pulses there are dangers in that short block pulses do

31
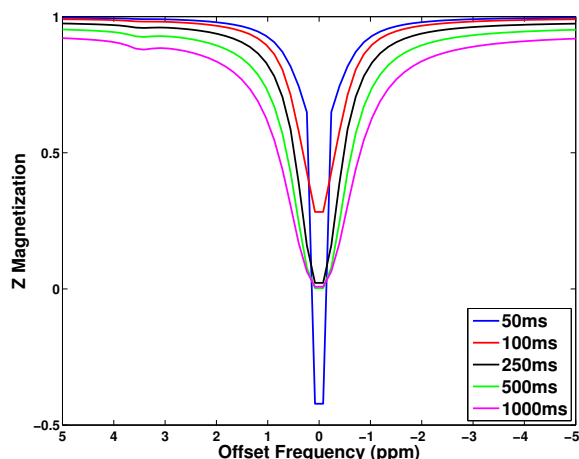
Fig. 4.9: Effect of Pulse Duration on the z-Spectrum for a CW Block Pulse

not allow the magnetization to reach a steady state and oscillations (called Rabi oscillations) occur causing non-physical values. We can see that increasing the pulse duration not only removes those oscillations, causing smoother curves, but we also see increase CEST contrast. Simulations as a function of $B_1$ amplitude (with pulse duration set to 3000 ms) from 1 $\mu$T to 3 $\mu$T (Figure 4.10) show that an increase in $B_1$ amplitude decreases the CEST contrast at 3.5p pm. This is an important simulation result as it has been shown that the maximal CEST contrast for a solute occurs when the saturation field is on the order of the exchange rate. For amide protons, which have exchange rate ~30-50 Hz, a pulse amplitude of 1 $\mu$T should, theoretically, give maximal CEST contrast.
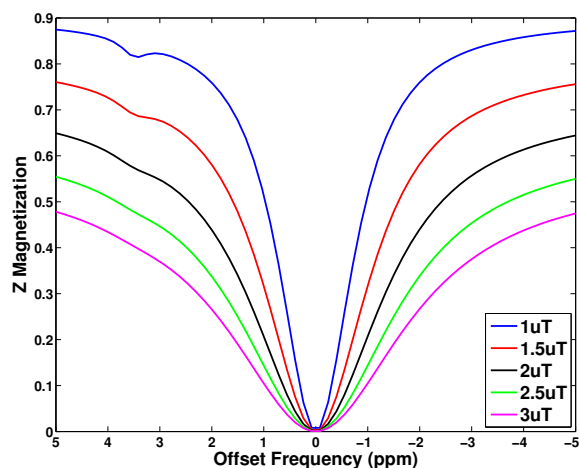


Fig. 4.10: Effect of $B_1$ Amplitude on the z-Spectrum for a CW Block Pulse

After these simulations, it can be clearly seen that a CW pulse as a saturation method is infeasible *in vivo* as the required pulse duration is beyond that of most scanners. In addition, the contrast that is achieved at even 1 second of continuous saturation is not enough to merit further consideration.

For a pulse train, there are four competing effects: pulse duration, pulse amplitude, number of pulses and duty cycle. As before, the shaped sinc-gauss pulse is used in the pulse train and pulsed scenarios due to the fact that a pulse train of short block pulses can introduce unnecessary oscillations (Figure 4.11).
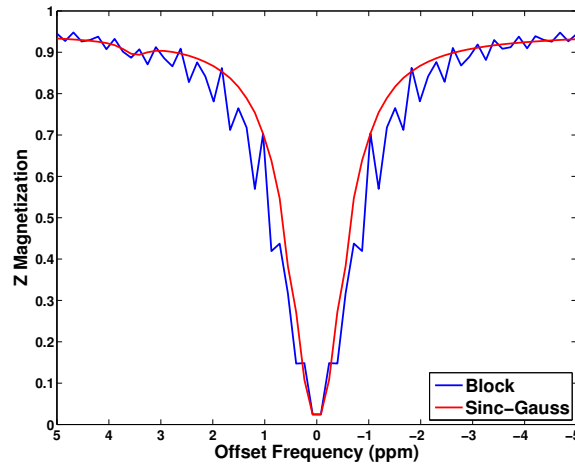


Fig. 4.11: Effect of Pulse Shape on the z-Spectrum for a Pulse Train

In order to test the pulse duration, the pulse amplitude was set to 1 $\mu$T and the number of pulses and duty cycle were set to 40 pulses and 50%, respectively. The pulse duration was then varied from 20 ms to 100 ms (Figure 4.12). From Figure 4.12, we can see the effect of the short pulse in widening the water peak through an increase in direct saturation and finite bandwidth. We see a return to the traditional lineshape as the duration increases, however, the CEST effect decreases with increased pulse duration. To test the effect of $B_1$ amplitude, forty 30 ms pulses were used at a 50% duty cycle and the $B_1$ amplitude was varied from 1 $\mu$T to 3 $\mu$T (Figure 4.13). In Figure 4.13, we can see the same results that we observed in the CW limit. The increased amplitude continues to cause broadening of the spectrum, due to increased direct saturation effect, and loss of CEST contrast due to the relationship between
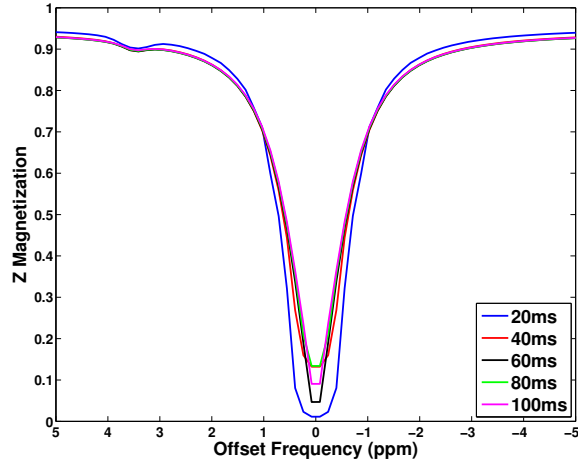
Fig. 4.12: Effect of Pulse Duration on the z-Spectrum for a Sinc-Gause Pulse Train
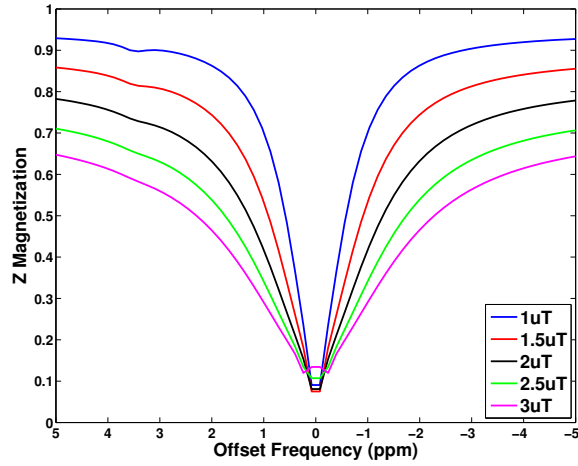


Fig. 4.13: Effect of $B_1$ Amplitude on the z-Spectrum for a Sinc-Gauss Pulse Train

the saturation field and the exchange rate. The next experiment used pulses 30 ms long with amplitude of 1 $\mu$T at a duty cycle of 50%, but the number of pulses was varied from 5 pulses to 40 pulses (Figure 4.14). Here we can see the slight broadening of the direct saturation lineshape, but we also see an increase in CEST effect as the saturation reaches steady state after a long number of pulses. This is additionally improved by decreasing the bandwidth of saturation, which results in less spectral smoothing. Finally, by using 40 pulses of 30 ms with amplitude of 1 $\mu$T, we are able to vary the duty cycle from 50% to 90% to measure its effect (Figure 4.15). This result is important in that for duty cycles ∼50%, a similar CEST effect can be seen indicating the ability to translate these findings to clinical hardware which restricts hardware demands to ∼50% duty cycle.
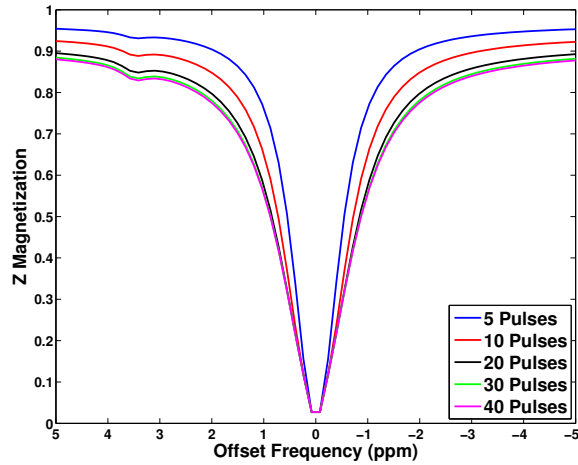
Fig. 4.14: Effect of Number of Pulses on the z-Spectrum for a Sinc-Gauss Pulse Train
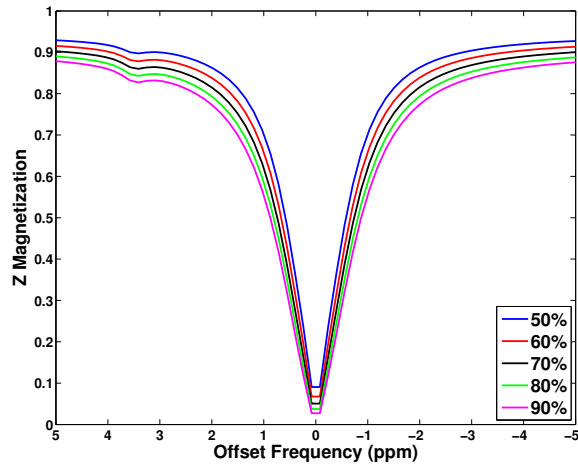


Fig. 4.15: Effect of Duty Cycle on the z-Spectrum for a Sinc-Gauss Pulse Train

After completing these simulations, we can see that a pulse train sequence may be practical due to the appearance of CEST contrast after shorter pulse trains. However, the contrast achieved after a train of 10 or 20 pulses is smaller than one would hope to achieve in an optimized scan. In addition, at a 60 ms pulse duration (which showed optimal spectral sensitivity and CEST effect) and a 50% duty cycle (which would be required on most scanners) the TR would be between 800 and 1600 ms, requiring extensive scan time to complete an entire range of offsets.

Lastly, we simulated the pulsed CEST approach by testing pulse duration, pulse amplitude and time to $k_0$. The $B_1$ amplitude was tested first by using 30 ms pulses for a time to $k_0$ of 2500 ms, then varying the $B_1$ amplitude from 1 $\mu$T to 3 $\mu$T (Figure 4.16). Here we see that for
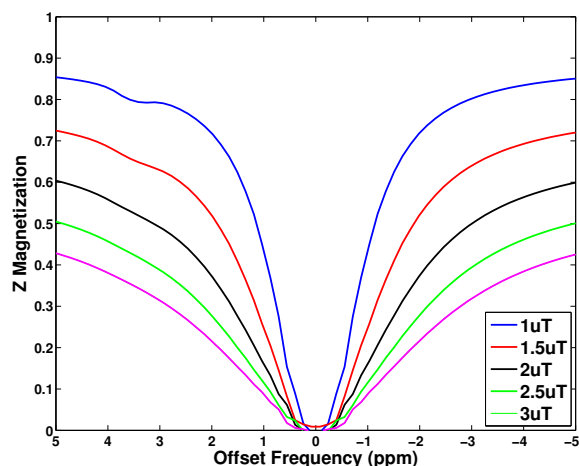
Fig. 4.16: Effect of $B_1$ Amplitude on the z-Spectrum for a Sinc-Gauss Pulsed Sequence

increasing pulse amplitudes the same significant line broadening and loss of the CEST effect is easily seen indicating, yet again, a desire for low power saturation. Next, the $B_1$ amplitude was held at 1 $\mu$T and 30 ms pulses were used, but the time to $k_0$ was varied from 500 ms to 2500 ms (Figure 4.17). As the time to $k_0$ increases, greater saturation is accumulated and a greater
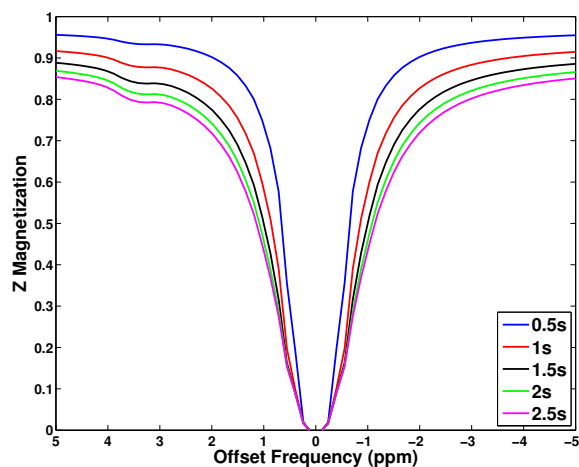


Fig. 4.17: Effect of Time to $k_0$ on the z-Spectrum for a Sinc-Gauss Pulsed Sequence

CEST effect can be seen compared to short approaches. Finally, the time to $k_0$ was held to 2500 ms and the $B_1$ amplitude was fixed to 1 $\mu$T while the pulse duration was varied from 20 ms to 60 ms (Figure 4.18). It is apparent that a short pulse is best for achieving sufficient CEST saturation.

Overall, these simulations show that for a pulsed CEST experiment sensitive to amide
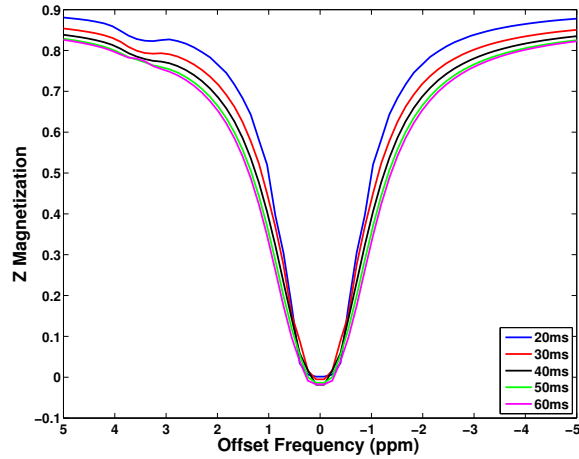
Fig. 4.18: Effect of Pulsed Duration on the z-Spectrum for a Sinc-Gauss Pulsed Sequence

protons (APT), a fairly short pulse ($\sim$30 ms), at 1-2 $\mu$T, and a long approach to $k_0$ is desirable to achieve maximal CEST contrast.

## 4.3   3D Simulations

In order to examine multiple variables at one time and to see the interaction that those variables might share, 3D plots were used to create a map of the CEST effect at various pulse parameters. First, a pulse train was simulated with 10, 30 and 50 pulses at a 90% duty cycle while varying pulse duration and pulse amplitude simultaneously (Figure 4.19). This shows the increase in CEST contrast as the number of pulses increases, as one would expect as the magnetization reaches its steady state. It also shows maximum values from 0.5 to 1.5 $\mu$T in the amplitude domain as well as 15 ms to 30 ms in the duration domain, which concurs with the findings in the above z-spectra simulations. It also shows that these maxima exist along a curve described in Figure 4.19. As smaller pulse durations will cause a bandwidth limiting spectral smoothing, it is feasible to take the minimum pulse duration that allows for frequency sensitivity (30 ms) and the $B_1$ value that corresponds to its maximum (0.75-1.25 $\mu$T).
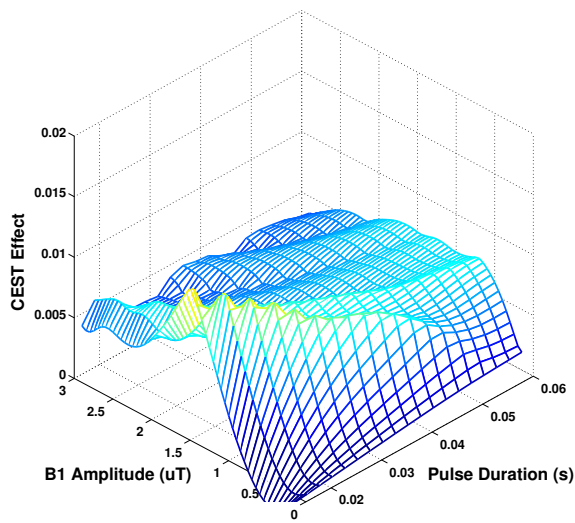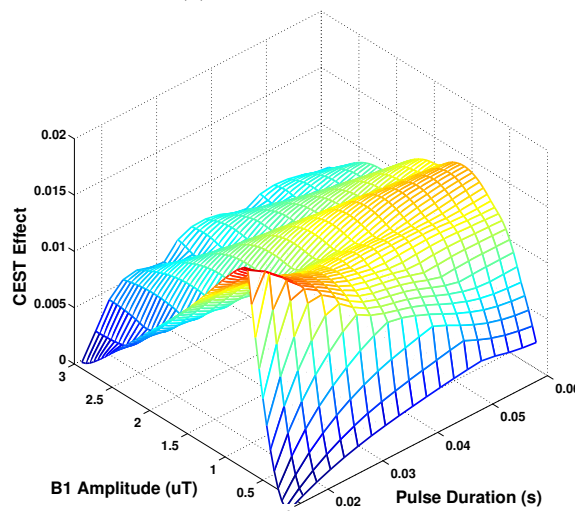
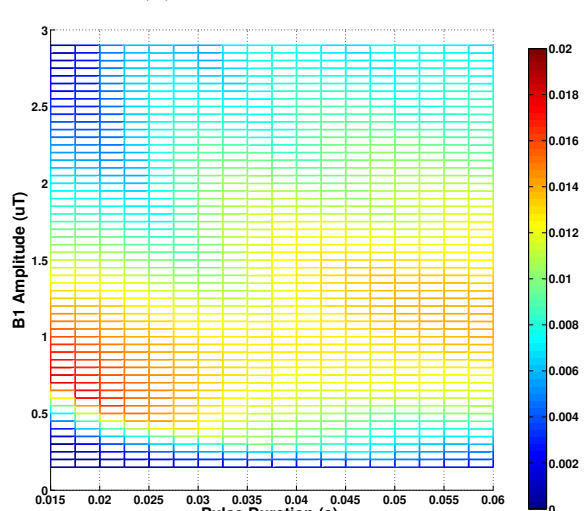(a) N = 10 Pulses (3D)
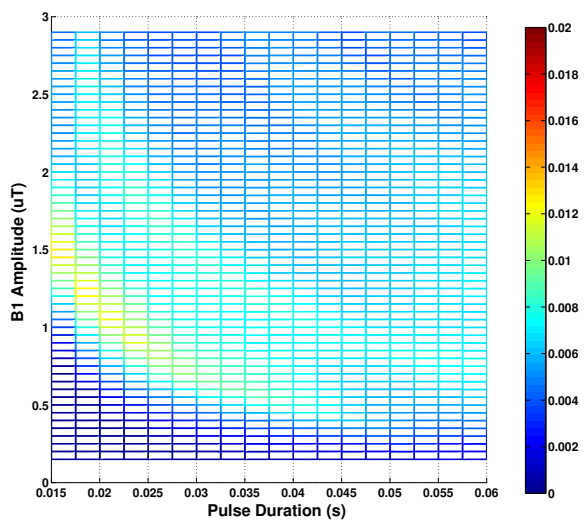
(b) N = 10 Pulses (XY-Plane)
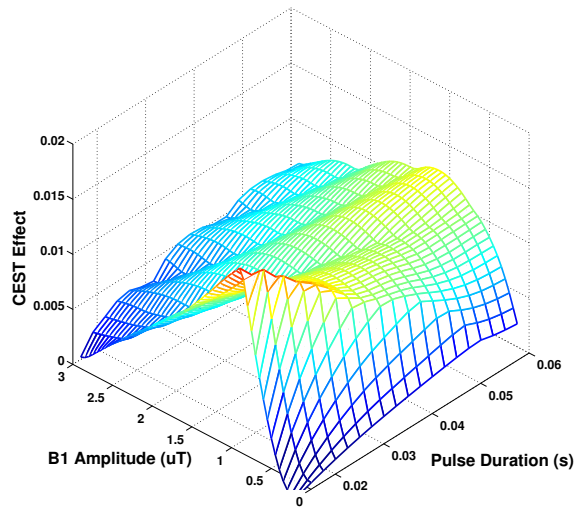
(c) N = 30 Pulses (3D)
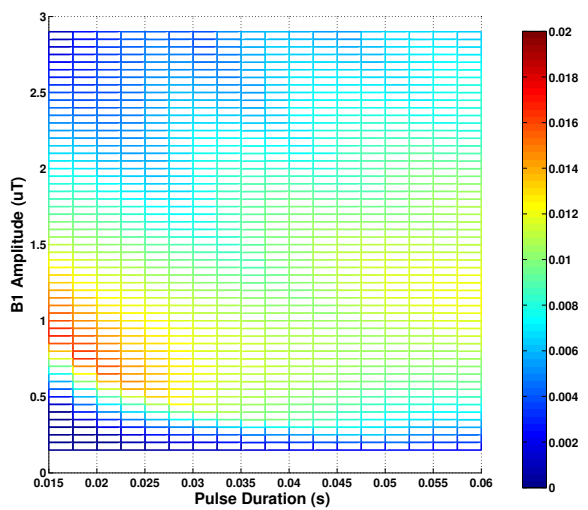
(d) N = 30 Pulses (XY-Plane)

(e) N = 50 Pulses (3D)

(f) N = 50 Pulses (XY-Plane)

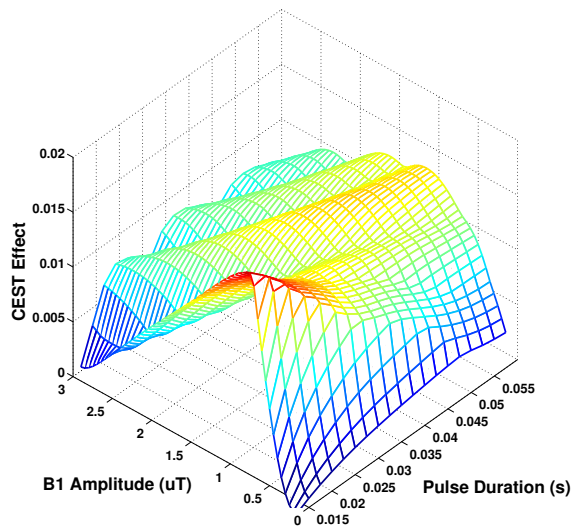Fig. 4.19: Comparison of 3D Plots for Pulse Trains with 10, 30, and 50 Pulses

In addition to number of pulses, the duty cycle was also tested to see its effect on the relationship between duration and amplitude of the pulse (Figure 4.20). To achieve this, the number of pulses was set to 50 and the duty cycle was set to 50%, 70% and 90% as shown in the figure. We can see that this plot is very similar to Figure 4.19, with the main differences being at higher values of amplitude and duration, far from the maximum values, where rippling is more evident in lower duty cycles because of added relaxation and oscillation that occurs.
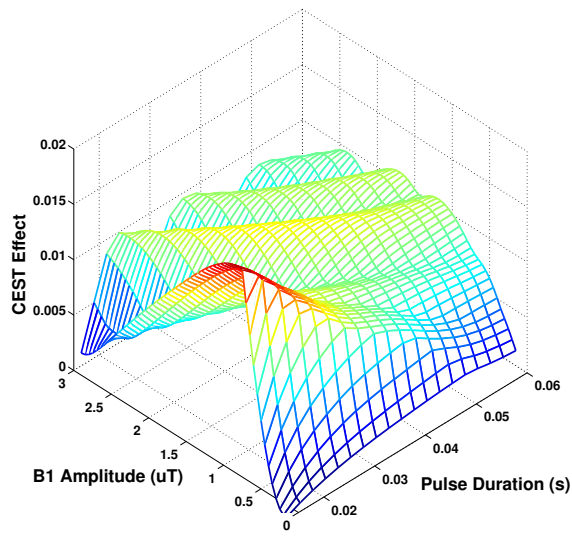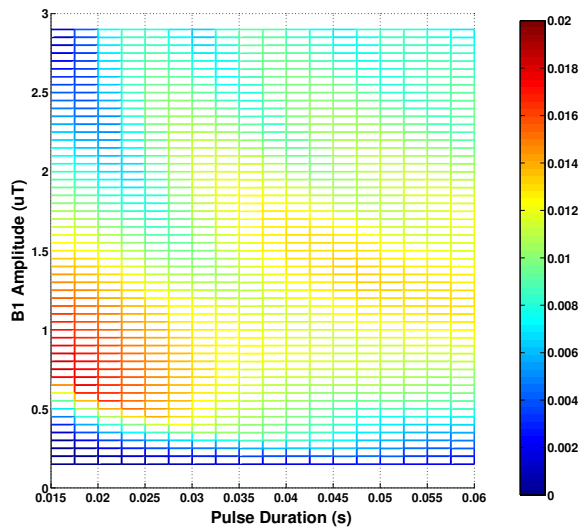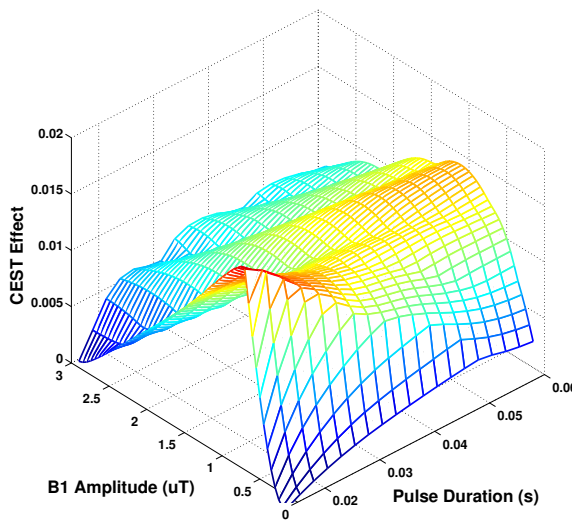
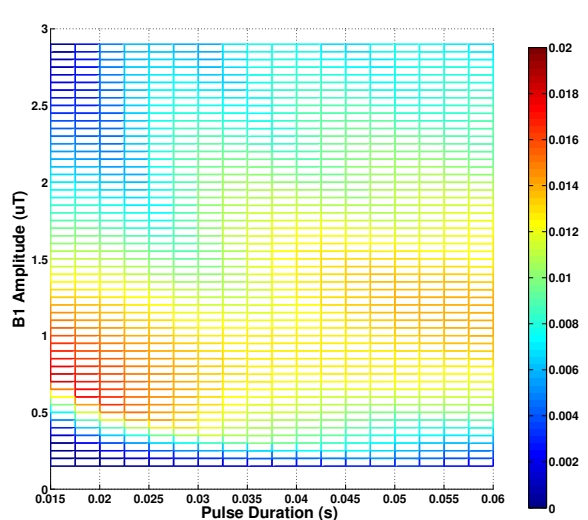(a) 50% Duty Cycle (3D)
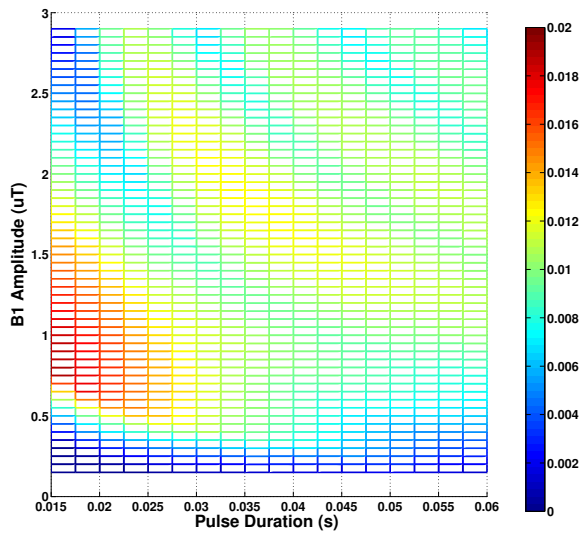
(b) 50% Duty Cycle (XY-Plane)

(c) 70% Duty Cycle (3D)

(d) 70% Duty Cycle (XY-Plane)

(e) 90% Duty Cycle (3D)

(f) 90% Duty Cycle (XY-Plane)

Fig. 4.20: Comparison of 3D Plots for Pulse Trains with 50%, 70% and 90% Duty Cycles

To examine 3D representations of the APT CEST effect from a pulsed CEST experiment, multiple plots were made based on the time to the center of k-space at 1 s, 3 s, and 5 s (Figure 4.21). Here we can see the maximum values that extend across the duration domain at an area within the range of 0.75 $\mu$T to 1.25 $\mu$T in the amplitude domain. In a comparison between plots, we see the broadening of this area in the amplitude direction, indicating a heightened CEST effect in the higher amplitude range, which occurs when approaching steady state. As in the pulse train experiments, we must also consider the effect of bandwidth, which is related to the inverse of the pulse duration. Here we can see that a shorter pulse will give greater contrast, but this is not feasible due to the bandwidth effect. Therefore, we must make the same decision as in the pulse train scenario and choose the lowest pulse duration that provides spectral sensitivity (30 ms) and use the amplitude values that result in the highest contrast (0.5 $\mu$T to 1.5 $\mu$T).
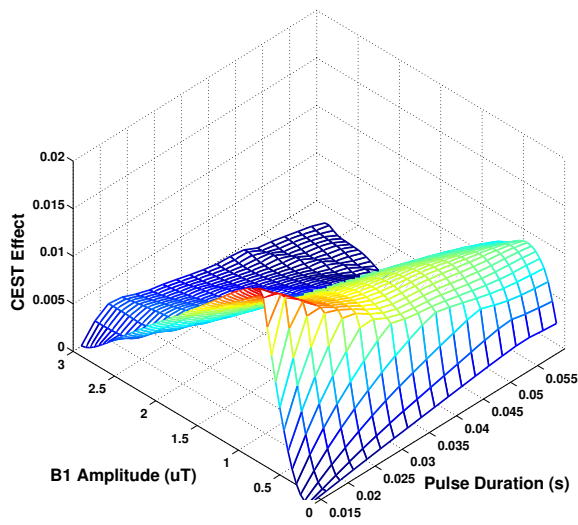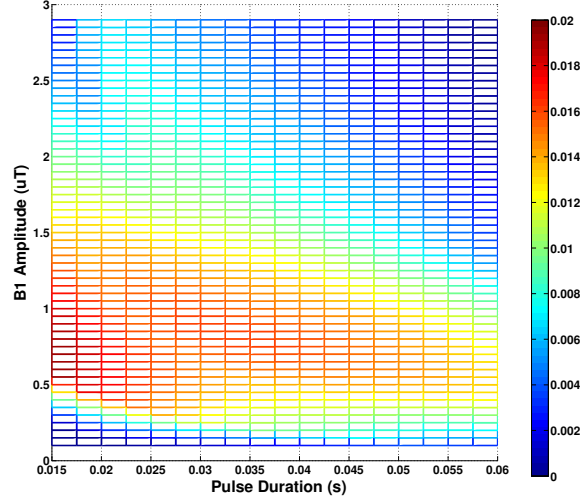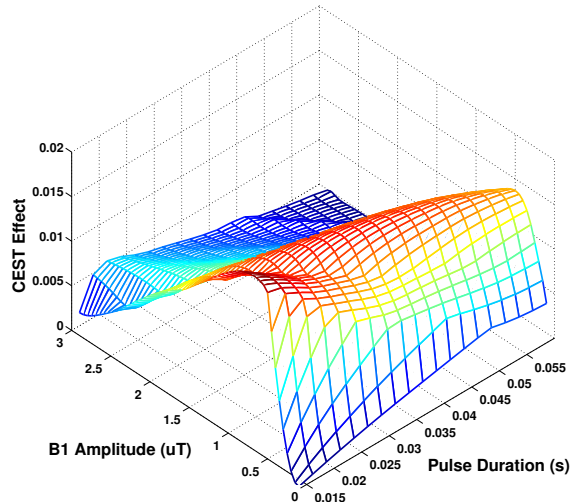
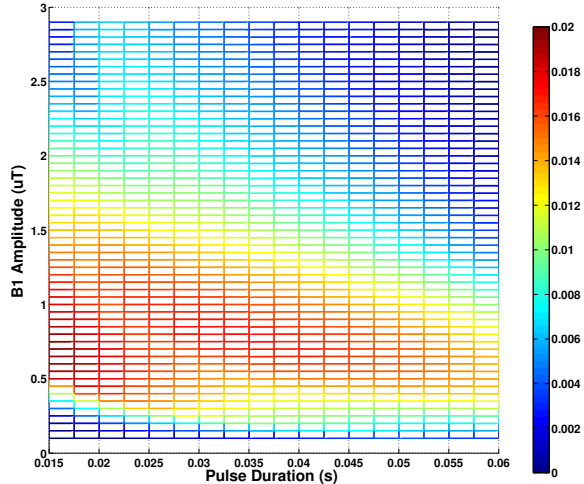(a) Time to $k_0 = 1$ s (3D)
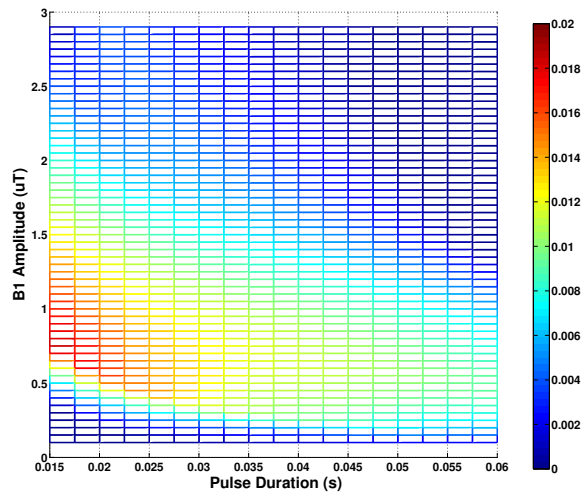
(b) Time to $k_0 = 1$ s (XY-Plane)
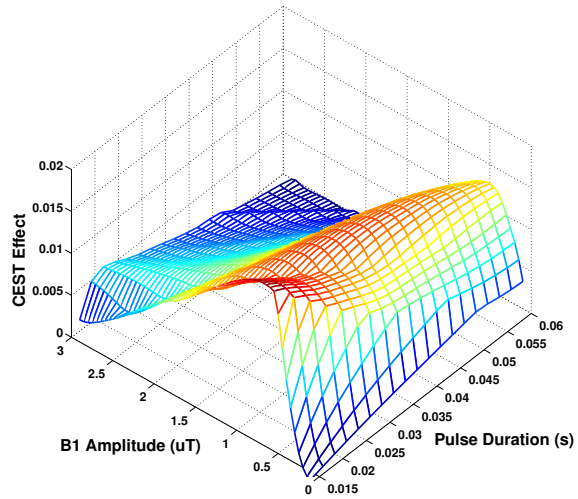
(c) Time to $k_0 = 3$ s (3D)

(d) Time to $k_0 = 3$ s (XY-Plane)
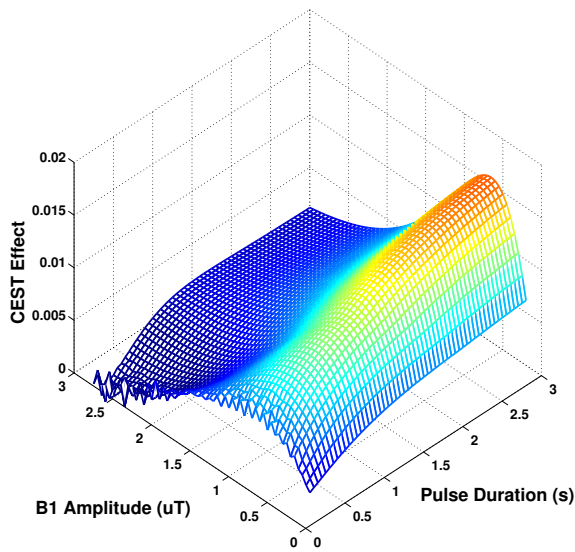
(e) Time to $k_0 = 5$ s (3D)
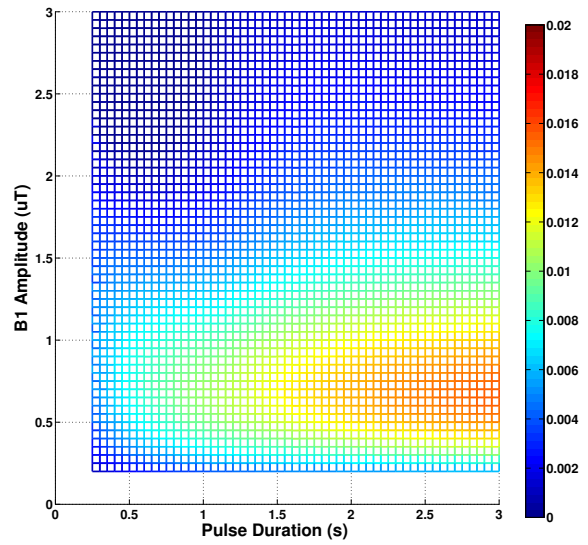
(f) Time to $k_0 = 5$ s (XY-Plane)

Fig. 4.21: Comparison of 3D Plots for Pulsed Sequences with Time to $k_0$ of 1, 3 and 5 s

Finally, the plots containing the highest CEST contrast from each of the pulse train and pulsed scenarios were compared to each other and to a CW block pulse that was simulated also simulated (250 ms to 3000 ms and 0.1 $\mu$T to 3 $\mu$T) (Figure 4.22). We can see that the CW example severely underperforms at any feasible values (<250 ms) and even suffers from oscillations in magnetization that occurs very far from steady state. We can also see that the pulsed sequence outperforms the pulse train sequence given similar pulse durations and amplitudes. This is in conjunction with the fact that a 50-pulse sequence would have a TR of a minimum of 750 ms on this plot, compared to the 30 ms in the pulsed sequence. From this we can clearly see that a simulated pulsed sequence using 1 $\mu$T and 30 ms for amplitude and duration, respectively, would give us the maximum contrast in the pulsed technique and overall. From this we can build a experimental environment to explore variables that cannot be tested in simulation.
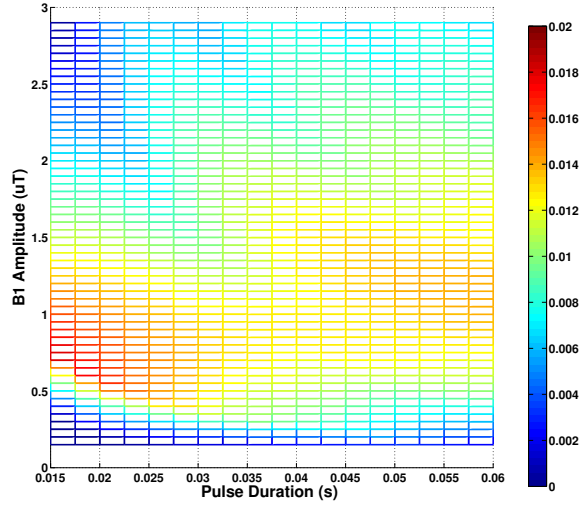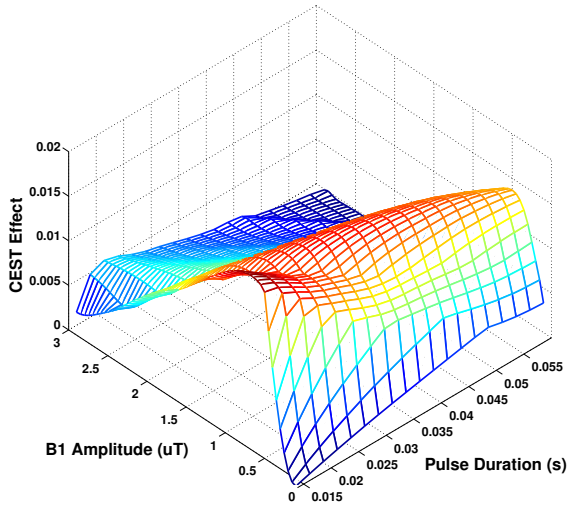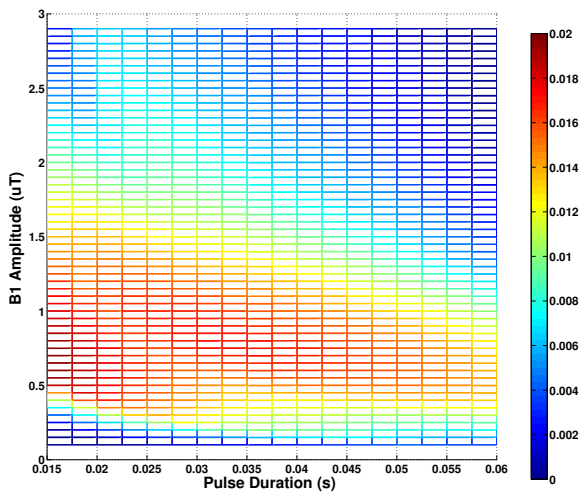
(a) CW Block Pulse (3D)

(b) CW Block Pulse (XY-Plane)
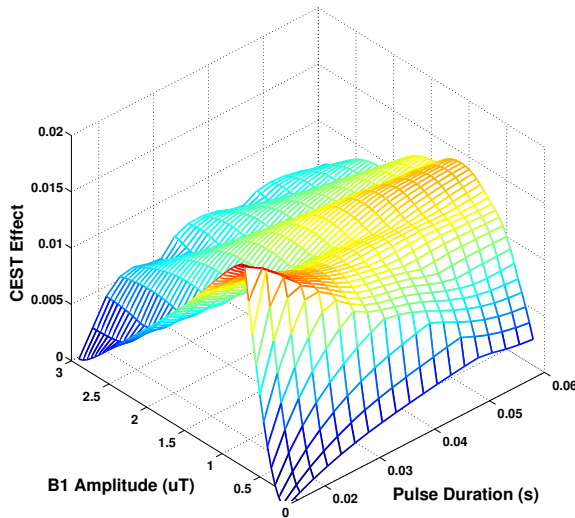
(c) Pulse Train with N = 50 and 90% Duty Cycle (3D)

(d) Pulse Train with N = 50 and 90% Duty Cycle (XY-Plane)

(e) Pulsed with Time to $k_0 = 5$ s (3D)

(f) Pulsed with Time to $k_0 = 5$ s (XY-Plane)

Fig. 4.22: Comparison of 3D Plots for Different Pulse Sequences

44

# CHAPTER 5
# Image Analysis

When calculating the CEST residual, the contrast that is derived from the data depends entirely on the fitting scheme and how the residual is defined. Over the course of the study, four fitting schemes were tested to determine which would give the best indication of CEST contrast with the least spillover from MT and other sources. In addition, each fitting scheme was tested to determine if it could accurately shift the data to place the minimum at 0 ppm ($B_0$ correction). It should be noted that no fitting scheme performed perfectly in the first regard and that further investigation is required to determine an effective scheme, however, each scheme was able to shift the data accurately to within the frequency sampling.

The first scheme that was evaluated was the One-Pool Lorentzian lineshape. This method fits a center, a width and a height for a Lorentzian curve (Equation 3.2, Figure 3.1a). This has the unfortunate consequence of not accounting for the contribution of MT, which is quite large in the pulsed CEST method (Figure 5.1a). Therefore, this fitting scheme was deemed inefficient in determining the CEST residual.

The next method, the Jones method adds a third fitting point to create a baseline and shift the Lorentzian down from one (Equation 3.3, Figure 3.1b). Unfortunately, the fitting algorithm in an attempt to minimize the error intersects the data at approximately 3.5 ppm (exactly where the APT resonance is). Therefore, some of the values on the APT map are negative when using this fitting method (Figure 5.1b). To correct for this, another constant term was added that created a maximum for the Lorentzian at the maximum value for the data, essentially 'tacking' the Lorentzian to the data. This provided promising results in controls of homogeneous contrast over the whole brain, which indicates that the MT effect has been

(a) One-Pool Lorentzian

(b) Jones Method

(c) Three-Pool Lorentzian
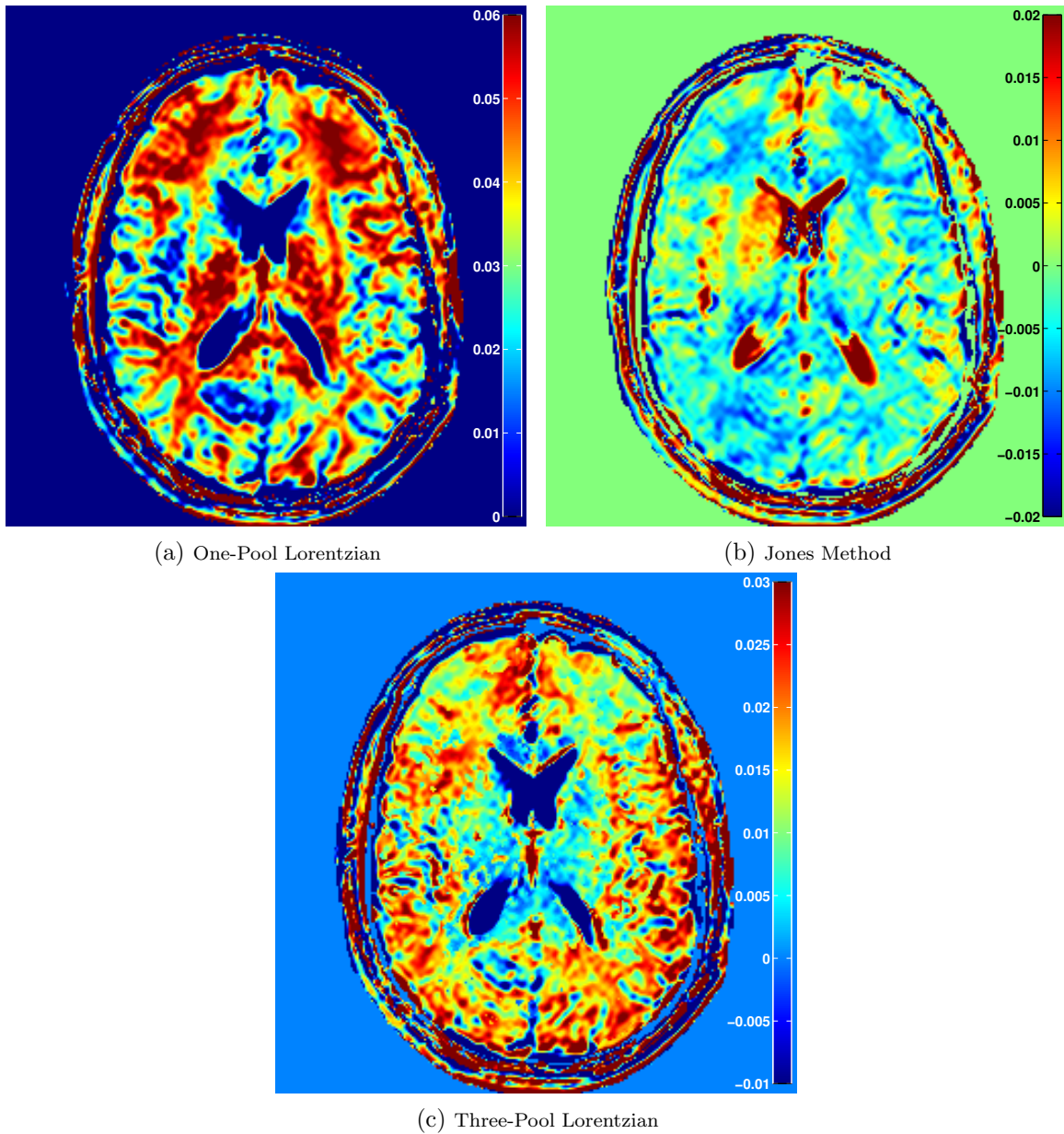
Fig. 5.1: Comparison of Fitting Methods Through APT Maps

successfully removed. The final method tested was the Three-Pool Lorentzian lineshape. This fits nine values (a center, width and height for each pool), but to calculate the residual, only the bulk water and MT pools are used so that the CEST effect can be extracted (Equation 3.5, Figure 3.1d). This method, while seeming to be the most complex still leaves some MT effect remaining in the APT residual signal (Figure 5.1c). With these results in mind, it was decided that the optimal fitting method was the 'tacked' Jones method as it effectively removed the MT effect from the APT signal. All of the residual analysis for this paper is done using this

technique unless otherwise noted.

In addition, a by-product of the 'tacked' Jones fit is a baseline value that is related to the MT effect present in that voxel. A map of these baseline values can be made and MT contrast is obtained without using an MT sequence (Figure 5.2). The CEST and MT map were obtained from the same control and when resolution (CEST 2x2x5 mm; MT 1.5x1.5x2.5 mm) is taken into account, show the same contrast. In this way, a 9-14 minute scan can really do the job of two scans that could total almost 30 minutes to run on their own according to previous standards.
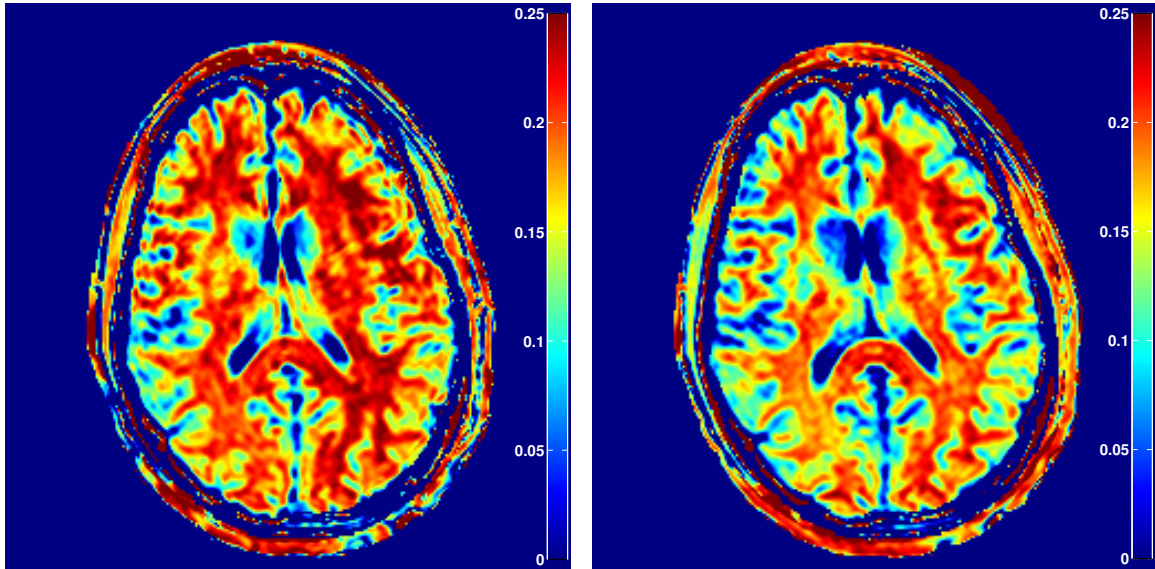
(a) Baseline 2 $\mu$T EPI Factor 11



(b) Baseline 2 $\mu$T EPI Factor 7
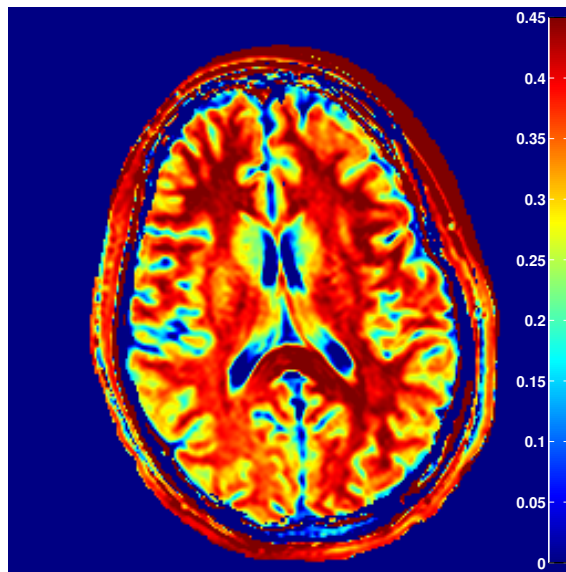


(c) MTR Map

Fig. 5.2: Comparison of Fitting Methods Through MT Maps

# CHAPTER 6

# *In Vivo* Scans

## 6.1   Control Scans

Using knowledge from our simulations, we chose to examine pulsed CEST acquisitions and implemented these in healthy control subjects. A pulse train sequence of forty 30 ms pulses at 1 $\mu$T and 50% duty cycle (determined from 3D simulations) was also included to justify, visually, the decision to use a pulsed CEST approach (Figure 6.1) . In addition to the long scan time (18 minutes for 3 slices), the pulse train is significantly lower SNR (Figures 6.1a and 6.1c) and the spectral quality is noisier than is the pulsed CEST approach (Figures 6.1b and 6.1d). Finally, various pulsed sequences were used to determine optimal settings (9-18 minutes).
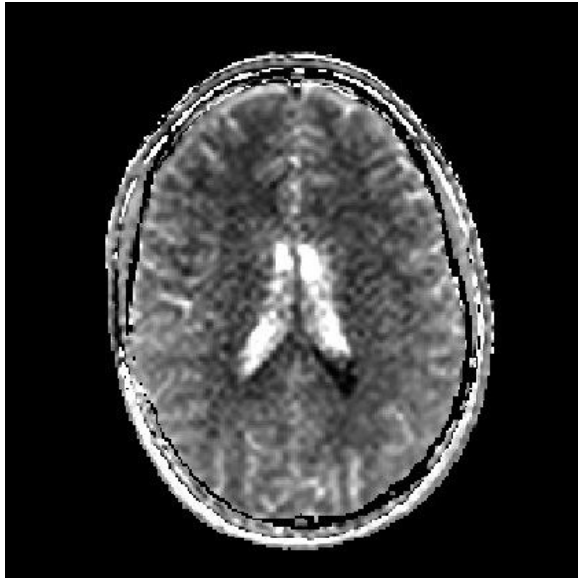
(a) Pulse Train CESTR Map (5 ppm)
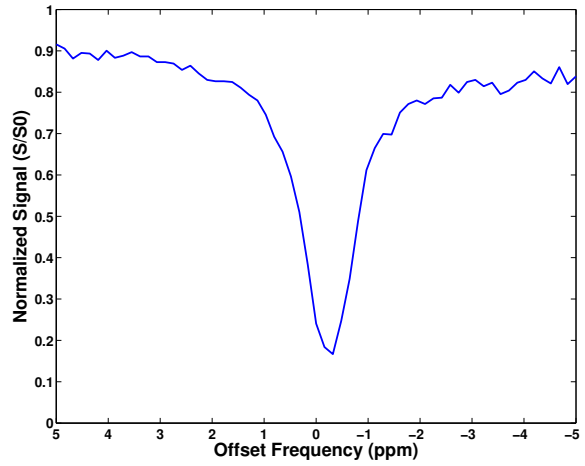
(b) Pulse Train Sample z-Spectrum
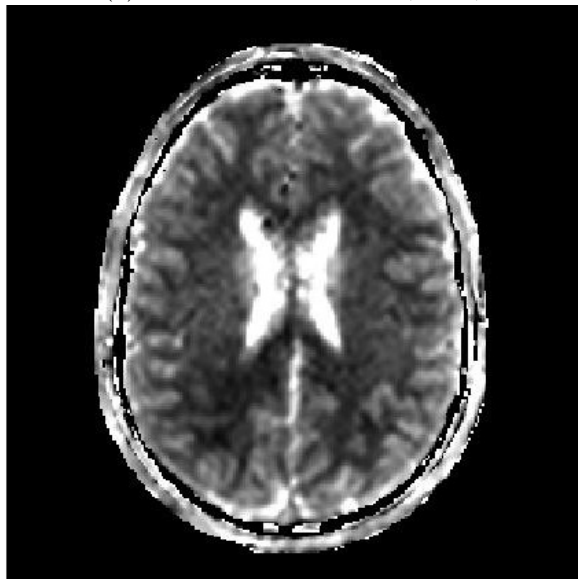
(c) Pulsed Sequence CESTR Map (5 ppm)
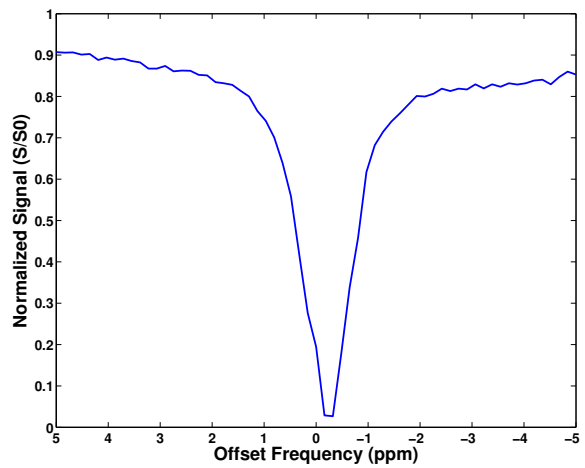
(d) Pulsed Sequence Sample z-Spectrum

Fig. 6.1: Comparison of Pulse Train and Pulsed Data

Over the course of the control scans, scans other than the experimental CEST sequences were to provide insight into the various phenomenon that appeared in the data. The first was a $T_1$ weighted MPRAGE sequence that allowed for segmentation of gray and while matter in the brain (Figure 6.2).



(a) $T_1$ Weighted MPRAGE Image

(b) Whole Brain ROI

(c) Gray Matter ROI

(d) White Matter ROI
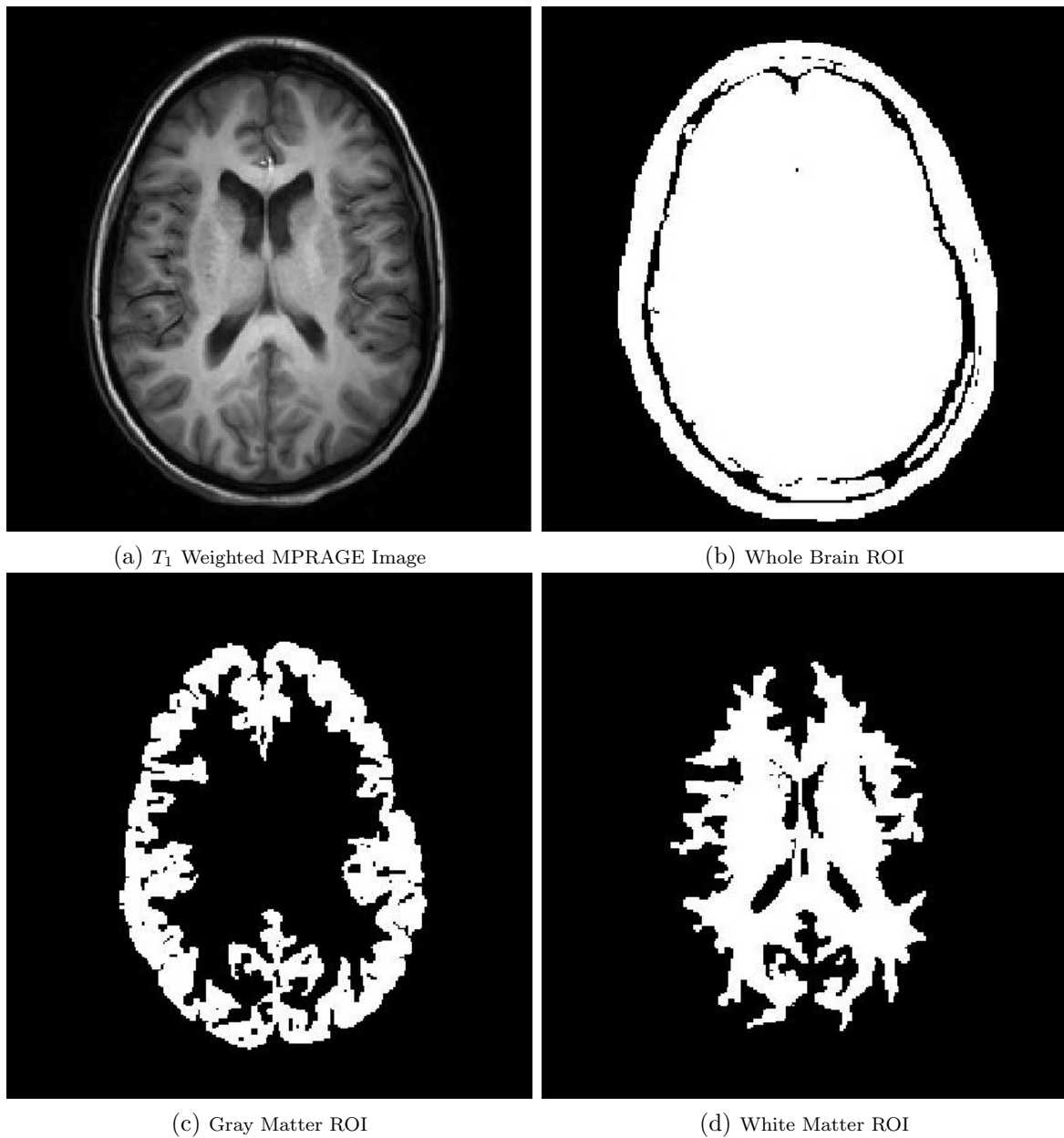
Fig. 6.2: Masking and Segmentation Images

Next was a $B_0$ map to compare with shifts done in the data analysis (Figure 6.3c). Finally, a $B_1$ map was obtained to gauge the magnitude of inconsistent saturation from the
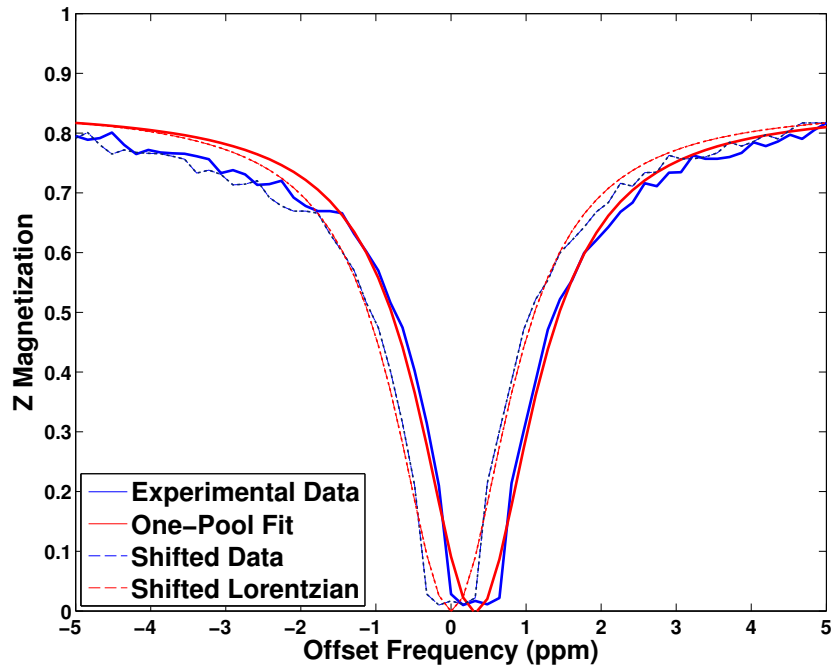


(a) Sample Shift
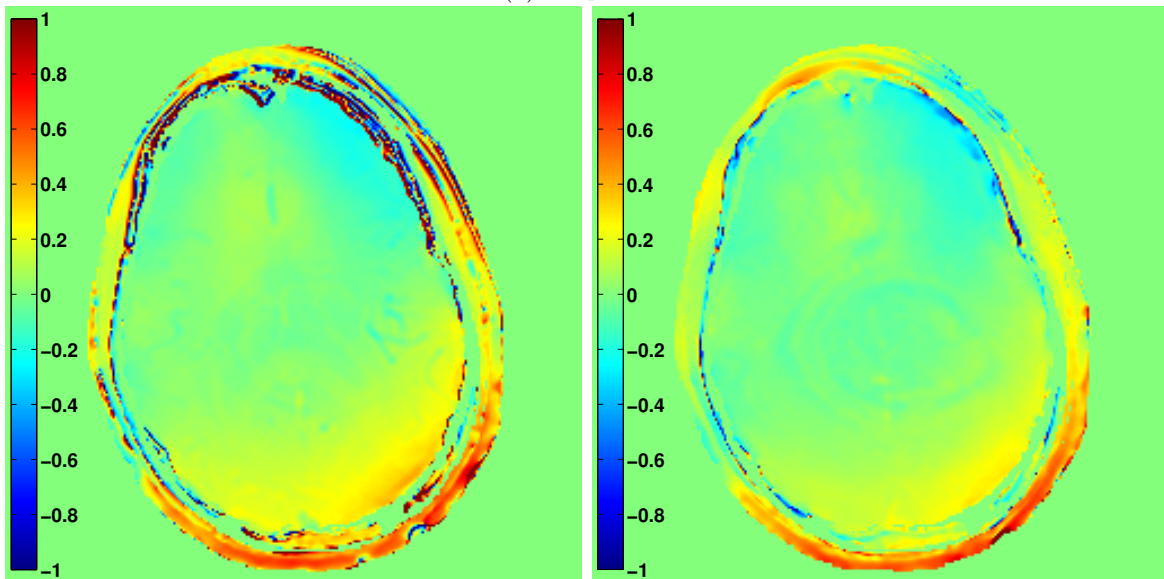


(b) Shift Map

(c) B0 Map

Fig. 6.3: B0 Correction Comparison

front to the back of the brain. (Figure 6.4). These scans together took less than 5 minutes of the scan protocol.
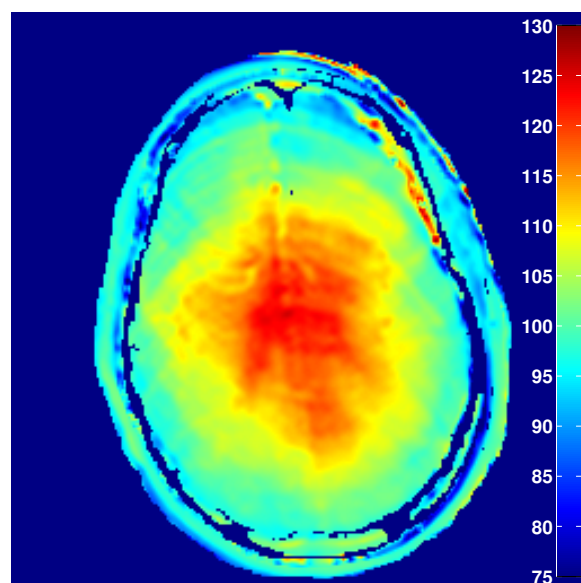
Fig. 6.4: Sample B1 Map

While the simulations provided the framework for optimized RF irradiation, pulse sequences were studied in healthy volunteers to provide an understanding of which readout schemes and which resolutions would be optimal for visualizing CEST contrast. First, a set of values for the pulse duration was determined by examining the 3D simulation for pulsed sequences, then the $B_1$ amplitude with maximum contrast for that pulse duration was chosen. These scans were then implemented on the same control (with a multi-shot EPI readout, EPI factor 11) to determine their feasibility. All scans were performed in 3D acquisition as this provides significantly slower approach to $k_0$ (and thus the magnetization is closer to steady state at the time $k_0$ is reached). Pulse duration values less than 25 ms were not optimal due to spectral smearing that is a result of the increased bandwidth associated with very short pulses. Pulse durations higher than 40 ms required an increase in $B_1$ amplitude to reach their maximum CEST contrast (which was decreased with pulsed duration anyways). For these reasons, the pulse duration of 30 ms was chosen from the spectra created from a single voxel placed in the anterior white matter (Figure 6.5). Next, the $B_1$ amplitude was altered to determine if the 1 $\mu$T described by the simulation would produce the best results. To determine this, 1 $\mu$T, 2 $\mu$T and 3 $\mu$T amplitudes were used on all further scans to determine the effect of each experiment on a each of the amplitude values. All of the scans described above were performed in 9 minutes for full brain coverage (20 slices of 5 mm thickness).

(a) 15 ms Pulse Duration

(b) 20 ms Pulse Duration

(c) 30 ms Pulse Duration

(d) 50 ms Pulse Duration

(e) 70 ms Pulse Duration
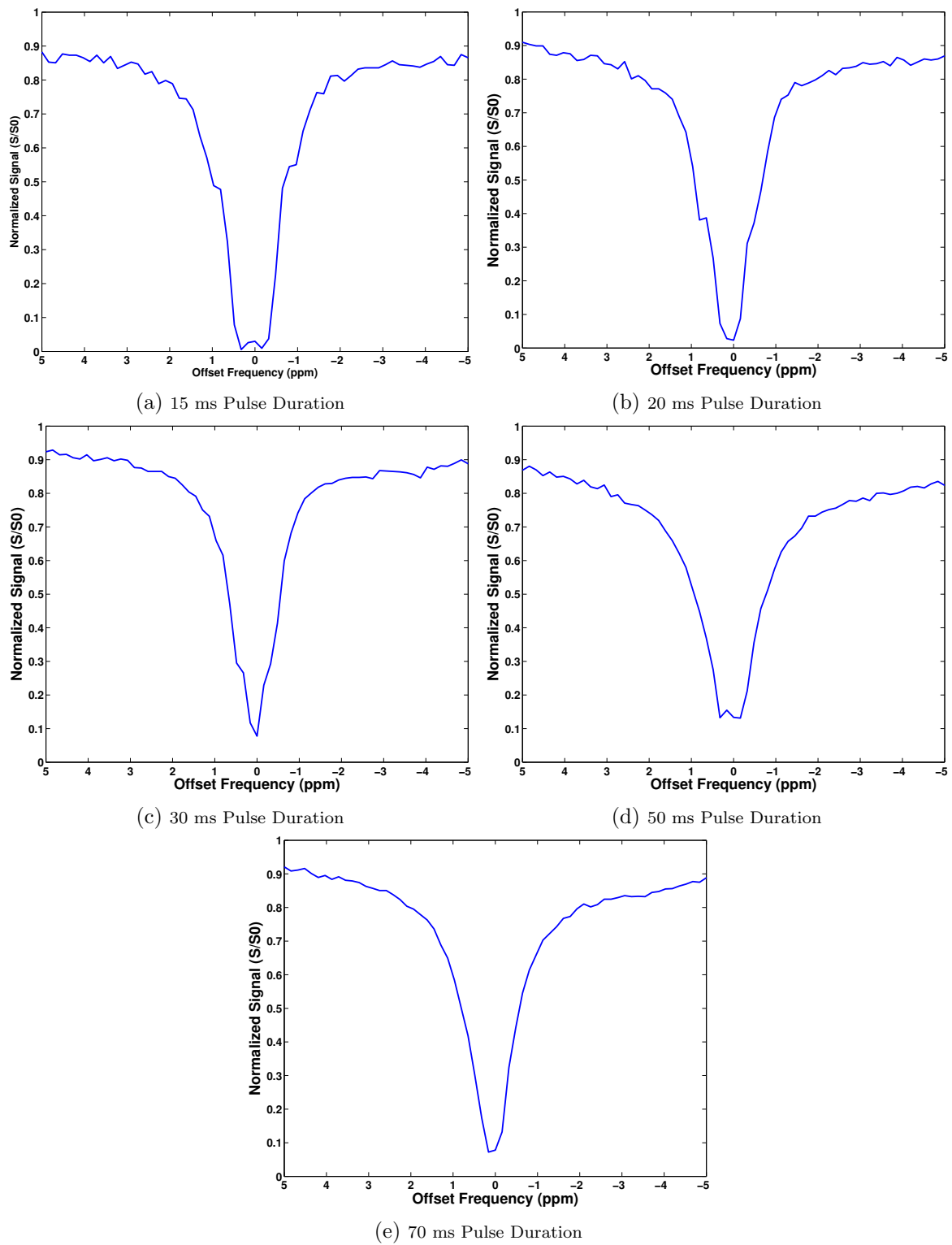
Fig. 6.5: Comparison of Pulse Durations for a Sinc-Gauss Pulsed Sequence

Due to low signal to noise (SNR) and the possibility of EPI related artifacts, multiple experiments were set up to determine the improvement that increased number of averages (NSA) or decreased EPI factor could offer a solution to each problem, respectively. As with any MRI optimization, these benefits must be weighed against the increased time that both options will require. The first experiment aimed to increase SNR by obtaining increasing the number of averages (NSA) to 2. This would increase the scan time twofold (18 minutes), but should provide cleaner, less noisy spectrums. While the z spectrum is less noisy, this does not increase the CEST contrast, only the overall signal of the volume. In fact, it also increases the signal in certain areas by amplifying fold-over artifacts, which is detrimental to the overall image (Figure 6.6). Therefore, we can conclude from this experiment that increasing the NSA to 2 would not improve the signal to a degree that merits the increase in scan time.

(a) 1 μT NSA=1

(b) 2 μT NSA=1

(c) 1 μT NSA=2

(d) 2 μT NSA=2
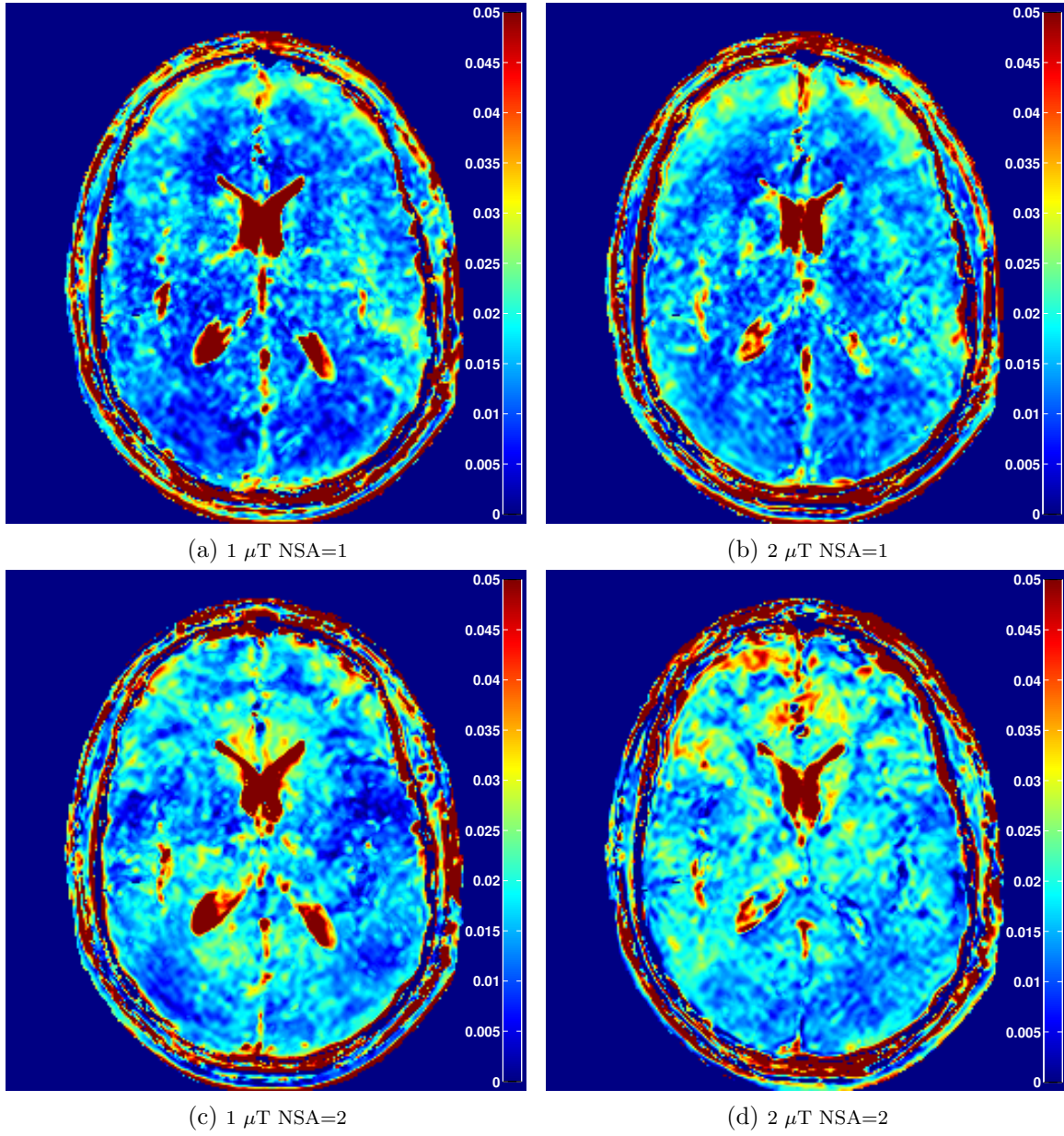
Fig. 6.6: Comparison of NSA Values Through APT Maps

Next, the EPI factor (number of lines of k-space per shot) was decreased to reduce EPI distortions and increase the time to $k_0$. For each $B_1$ amplitude, EPI factor 11 and EPI factor 7 were both obtained and as we observed increased homogeneity in the signal for 2 $\mu$T in the EPI factor 11 and EPI factor 7 results, EPI 9 was obtained for 2 $\mu$T. In this experiment, there is a notable improvement in contrast as the EPI 7 images provide a more homogeneous signal anterior to posterior, eliminating some of the contamination at the anterior part of the brain (Figure 6.7). We can also conclude from this experiment that at EPI factor 7, the 2 $\mu$T amplitude pulse gives the most homogeneous map and would be optimal for CEST acquisition (Figure 6.8).
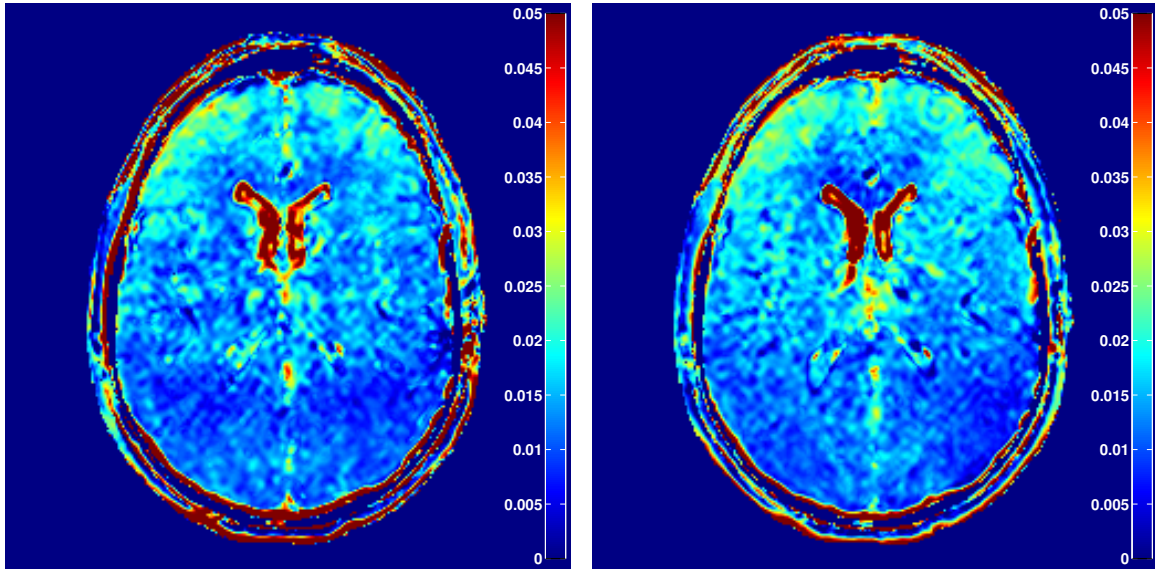
(a) 2 $\mu$T EPI Factor 11

(b) 2 $\mu$T EPI Factor 9
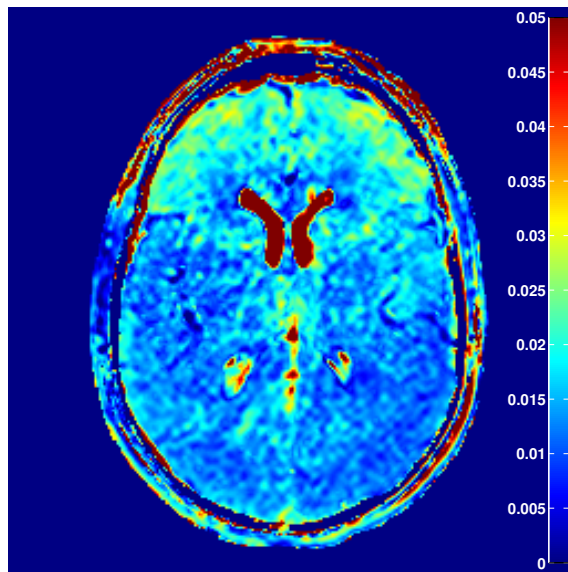
(c) 2 $\mu$T EPI Factor 7

Fig. 6.7: Comparison of EPI Factor Through APT Maps

After all simulations and experiments were completed, we found the optimal contrast to be obtained by using a 30 ms long, 2 $\mu$T pulse acquired using the pulsed CEST method with an EPI factor of 7 and one signal average obtained.



(a) 1 $\mu$T

(b) 2 $\mu$T

(c) 3 $\mu$T
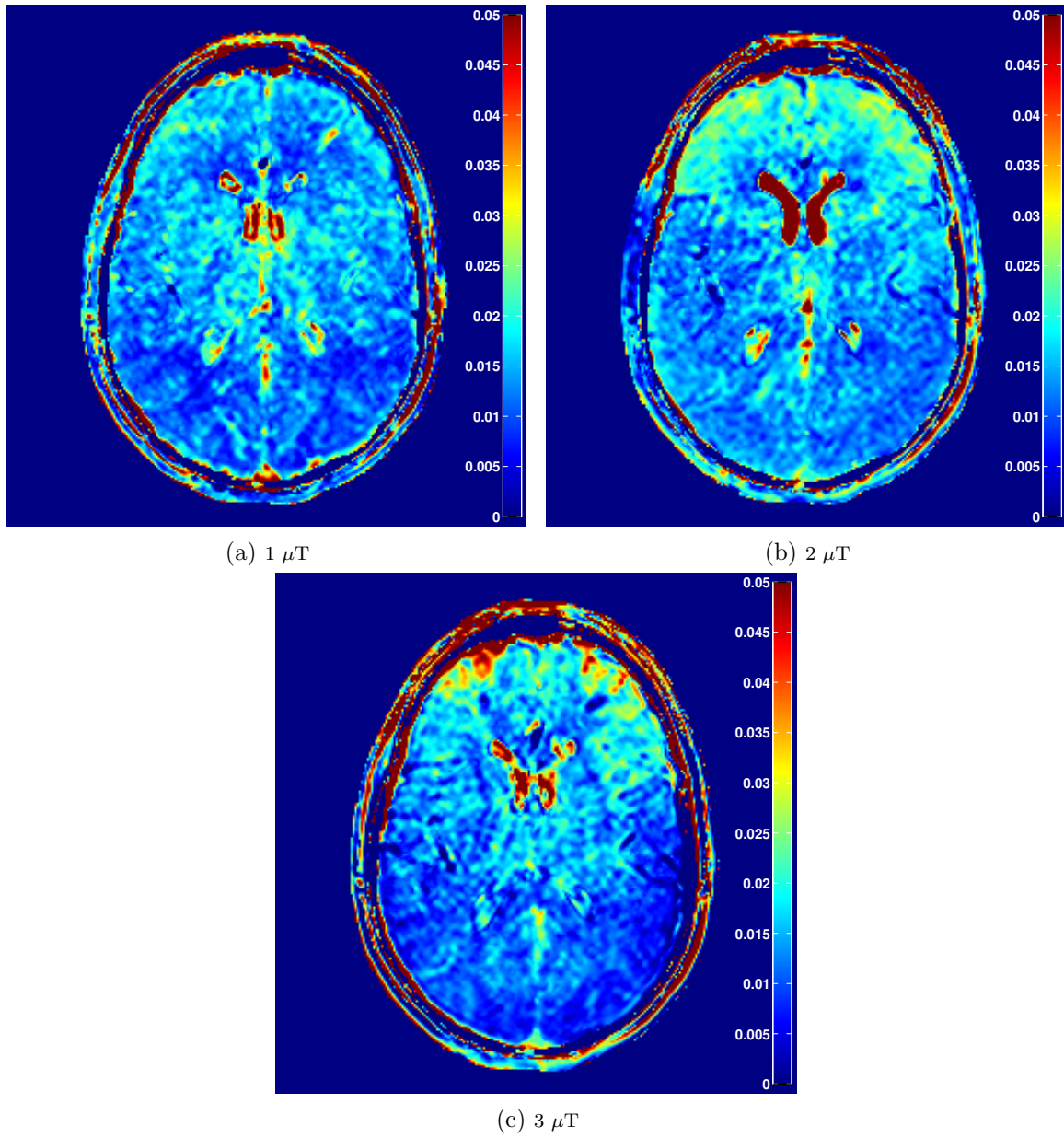
Fig. 6.8: Comparison of $B_1$ Through APT Maps

## 6.2 Multiple Sclerosis Patient Scan

It is important to note that in healthy volunteers, the CEST effect at 3.5 ppm (i.e. the APT effect) is not expected to have dramatic contrast between WM and GM. However, it has been shown by Zhou et al that in tumors, the contrast in the CEST images are significantly different compared to healthy volunteers[25]. At this point, we have optimized a pulsed CEST acquisition through simulation and in healthy volunteers. We then tested this pulse sequence on a patient with relapsing remitting multiple sclerosis (RRMS). One of the hallmarks of RRMS is large demyelinating lesions and so-called dirty white matter, which is thought to arise from dysmeylination rather than demyeliation. We hypothesize that APT CEST may be able to characterize patients with MS and show differences with respect to healthy volunteers. In this patient (Age 34, Male), we used a 30 ms RF irradiation at 2 $\mu$T pulse with EPI factor = 7 (TR/TE/a = 65 ms/7.5 ms/19 degrees, SENSE = 2 in AP encode direction, Resolution = 2x2x5 mm, scan time = 9.5 minutes). In addition, a $T_1$-weighted MPRAGE, $B_1/B_0$ field maps, and a MTR sequence were all played out in order to conduct the same tests as performed in the control groups.

The $T_1$-weighted anatomical scan provided clear representation of the lesions (arrows) and allowed segmentation of those lesions. Due to signal depression within lesions, the initial segmentation wrongly categorized the lesions as gray matter, requiring manual segmentation of the lesions in order to reincorporate them into the white matter mask. By performing the same Lorentzian analysis, APT and baseline maps were created and compared against the anatomical image to determine signal change within the lesions.

(a) Anatomical MPRAGE (Lesions Marked)

(b) APT Map

(c) Lorentizian Fitting Baseline

(d) MTR Map
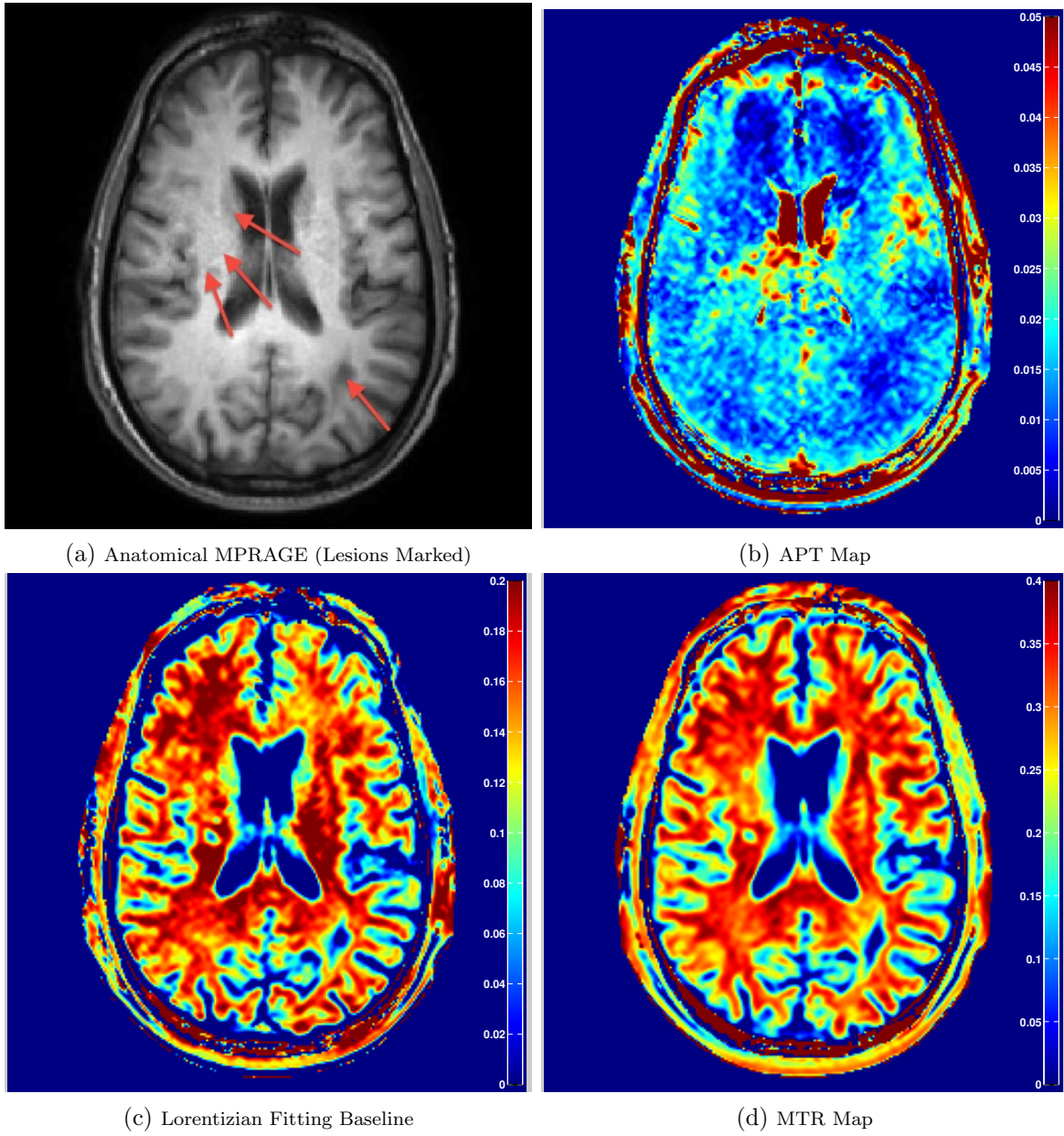
Fig. 6.9: Maps Created from MS Patient CEST Results

From the CEST APT maps, we see substantially lower CEST effect in the left posterior periventricular white matter proximal to the optic radiation and in the bilateral frontal white matter. Additionally in the right medial aspect of the lateral ventricles we see a signal elevation in the CEST effect concomitant with an elevation in the left parietal juxtacortical white matter. Interestingly, when examining the MTR, this later region shows a very high MT effect. The lesions lateral to the lateral ventricles show a MTR decrease, but not as much as the left posterior lesion. It should also be pointed out that the baseline image that is created from the Lorentzian analysis mimics the MTR maps in a number of ways and thus could be used as an MTR surrogate from a CEST acquisition. In addition to the analysis between lesion



(a) Mean z-Spectra from Patient Data

(b) Mean z-Spectra from Control Data

(c) Patient APT Effect Histogram

(d) Control APT Effect Histogram
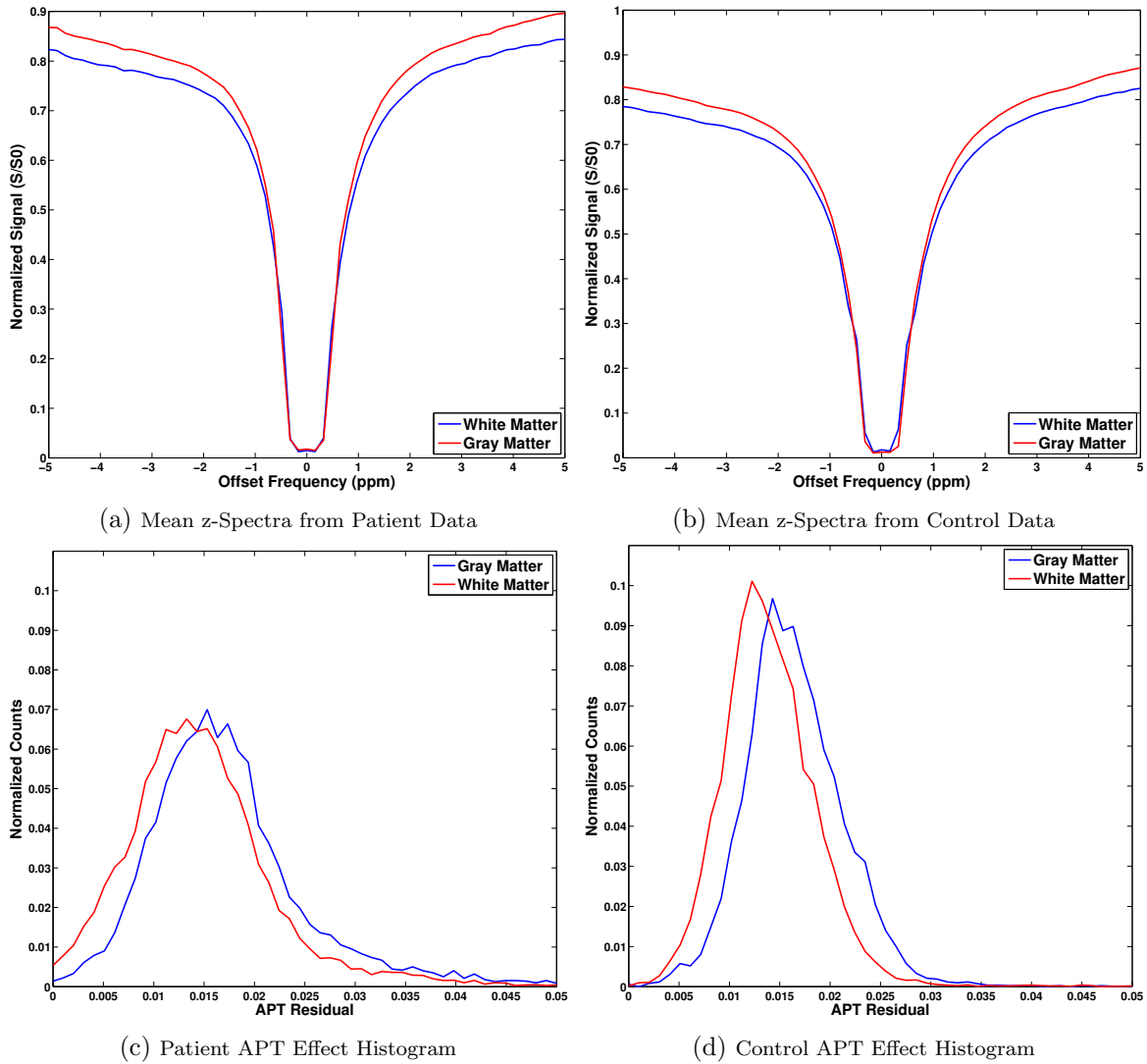
Fig. 6.10: Spectra Created from MS Patient CEST Results

and non-lesion tissue within the patient brain, an analysis was also done to compare a healthy control to the patient data. From an analysis of the average z-spectra of white and gray matter, we can see lower signal values in the control data. In a histogram analysis of the white and gray matter, we can see considerable spreading of white and gray matter histograms, while the overall shape of the curve and shift in the curve peaks remains the same.

# CHAPTER 7
# Discussion

This study showed that CEST MRI images could be obtained within clinical scan time constraints (9-14 minutes depending on EPI factor). In order to best investigate the phenomenon that govern CEST contrast, this study began from the very most basic mathematical derivations, the Bloch equations. From there, adaptable simulations were created to give theoretical data on each of the three pulse sequence types: CW, pulse train and pulse. By beginning with simulated data on all possible pulse types, theoretical optimization was used to determine the pulse parameters that give maximum CEST contrast for each pulse type. It is important to point out that while the data seems similar to what we would expect we cannot model all of the interacting effects with any accuracy. For this reason, some phenomenon that occur in simulation will never occur in vivo and vice versa.

The next step of the optimization process was to begin experimental trials *in vivo* to determine if the theoretical values would be consistent with data obtained in a healthy control. When presented with scanner restrictions, these theoretical maximums had to be tempered (at least in the CW and pulse train regimes) to accommodate RF amplifier and SAR restrictions as well as time constraints on the pulse train scan. The two largest reasons that these would not produce high quality images are the single-shot EPI sequence that is required to keep scan time down and insufficient saturation in the CW case and to some degree in the pulse train case. In the pulsed scenario, the main concern was spectral smearing as a result of short pulse duration. For this reasons some of the short pulse maximums had to be disregarded in order to achieve adequate sampling in the frequency domain.

The $B_1$ amplitude was varied throughout the study in an attempt to find an optimal value.

From the 1 $\mu$T, 2 $\mu$T and 3 $\mu$T trials, the 2 $\mu$T was determined to be the optimal because it shows the most homogeneous contrast over the entire brain without significant anterior brightening or posterior darkening (Figure 6.8). This contrast change in the extreme anterior and posterior is likely due to fold over from the sinus cavities combined with $B_1$ inhomogeneity. In addition, the 2 $\mu$T baseline image shows the closest contrast to the MT image, indicating that a 2 $\mu$T pulse is optimal to recover MT contrast from the CEST data.

Finally, the examination of multiple fitting algorithms allowed this study to determine the best (although not perfect) fitting scheme for the z-spectrum. By adding a baseline and another 'tacking' constant to a standard Lorentzian lineshape, a reasonable fit can be obtained that will produce a residual with homogeneous contrast in the brain. In addition to providing the CEST residual, this fit provides a baseline that compares to a MT ratio map. This would allow one shorter scan to take the place of two longer scans, which in the clinical setting would boost performance considerably.

# Chapter 8
# Conclusion

This study successfully optimized a pulsed CEST sequence in the human brain at 3T. This sequence consists of at 30 ms saturation prepulse with a peak amplitude of 2 $\mu$T followed by fat saturation binomial (1331) pulse and one shot of a multi-shot readout. 63 dynamics were taken from -5 to 5 ppm relative to water and one baseline reading was taken far off-resonance of water ($\sim$80000 ppm). This data was then reconstructed on the scanner and then analyzed using Matlab. The CESTR was calculated and the 'tacked' Jones method was used to fit a Lorentzian to each voxel within the brain. The data was then shifted according to the center of the fitted Lorentzian. The residual was calculated by subtracting the shifted CESTR from the shifted, fitted Lorentzian. The area under the residual was calculated for the 2 adjacent points on either side of the resonance frequency and the resonance frequency. While this fitting method was deemed the most successful at eliminating confounding effects, there is still room for improvement in Lorentzian fitting. From this protocol, we were able to isolate CEST contrast in healthy controls as well as in RRMS. We saw a homogeneous white and gray matter distribution in the healthy controls and saw changes congruent with established tendencies in the MTR map in RRMS. In addition, we found that fitting for the CEST spectra established a baseline that is comparable to an MTR map in its own right. This allows for simultaneous acquisition of both MTR and CEST.

# APPENDIX A

# TR Calculations Based on SAR Models

| Pulse Duration (ms) | $B_1$ ($\mu$T) | TR (ms) | Pulse Duration (ms) | $B_1$ ($\mu$T) | TR (ms) |
|---|---|---|---|---|---|
| 5 | <4.75 | 20 | 25 | <4.75 | 55 |
| 5 | 5.00 | 20 | 25 | 5.00 | 55 |
| 5 | 5.25 | 20 | 25 | 5.25 | 61 |
| 5 | 5.50 | 20 | 25 | 5.50 | 67 |
| 5 | 5.75 | 20 | 25 | 5.75 | 73 |
| 5 | 6.00 | 20 | 25 | 6.00 | 79 |
| 10 | <4.75 | 25 | 30 | <4.75 | 65 |
| 10 | 5.00 | 25 | 30 | 5.00 | 66 |
| 10 | 5.25 | 25 | 30 | 5.25 | 73 |
| 10 | 5.50 | 27 | 30 | 5.50 | 80 |
| 10 | 5.75 | 29 | 30 | 5.75 | 87 |
| 10 | 6.00 | 32 | 30 | 6.00 | 95 |
| 15 | <4.75 | 35 | 35 | <4.75 | 75 |
| 15 | 5.00 | 35 | 35 | 5.00 | 77 |
| 15 | 5.25 | 37 | 35 | 5.25 | 85 |
| 15 | 5.50 | 40 | 35 | 5.50 | 93 |
| 15 | 5.75 | 44 | 35 | 5.75 | 101 |
| 15 | 6.00 | 48 | 35 | 6.00 | 110 |
| 20 | <4.75 | 45 | 40 | <4.75 | 85 |
| 20 | 5.00 | 45 | 40 | 5.00 | 88 |
| 20 | 5.25 | 49 | 40 | 5.25 | 97 |
| 20 | 5.50 | 54 | 40 | 5.50 | 106 |
| 20 | 5.75 | 59 | 40 | 5.75 | 116 |
| 20 | 6.00 | 64 | 40 | 6.00 | 126 |

| Pulse Duration (ms) | $B_1$ ($\mu$T) | TR (ms) |
|---|---|---|
| 45 | <4.75 | 96 |
| 45 | 5.00 | 99 |
| 45 | 5.25 | 109 |
| 45 | 5.50 | 119 |
| 45 | 5.75 | 130 |
| 45 | 6.00 | 141 |
| 50 | <4.75 | 106 |
| 50 | 5.00 | 109 |
| 50 | 5.25 | 120 |
| 50 | 5.50 | 132 |
| 50 | 5.75 | 144 |
| 50 | 6.00 | 157 |
| 55 | <4.75 | 116 |
| 55 | 5.00 | 120 |
| 55 | 5.25 | 132 |
| 55 | 5.50 | 145 |
| 55 | 5.75 | 158 |
| 55 | 6.00 | 172 |
| 60 | <4.75 | 126 |
| 60 | 5.00 | 131 |
| 60 | 5.25 | 144 |
| 60 | 5.50 | 158 |
| 60 | 5.75 | 173 |
| 60 | 6.00 | 188 |

# References

[1] William R. Hendee and E. Russell Ritenour. *Medical Imaging Physics.* John Wiley & Sons, Inc., 2002. 1, 6

[2] R M Henkelman, G J Stanisz, and S J Graham. Magnetization transfer in mri: a review. *NMR Biomed*, 14(2):57–64, Apr 2001. 1

[3] Thomas E. Yankeelov, David R. Pickens, and Ronald R. Price. *Quantitative MRI in cancer.* CRC press, Boca Raton, 2012. 1

[4] S D Wolff and R S Balaban. Magnetization transfer contrast (mtc) and tissue water proton relaxation in vivo. *Magn Reson Med*, 10(1):135–44, Apr 1989. 1

[5] Seth A Smith. *Development of MR Saturation Techniques to Detect and Quantify Macromolecular Pathologies Afflicting the Brain and Spinal Cord.* PhD thesis, Johns Hopkins University, 2006. 2, 3

[6] K M Ward, A H Aletras, and R S Balaban. A new class of contrast agents for mri based on proton chemical exchange dependent saturation transfer (cest). *J Magn Reson*, 143(1):79–87, Mar 2000. 2

[7] Jinyuan Zhou, Bachchu Lal, David A Wilson, John Laterra, and Peter C M van Zijl. Amide proton transfer (apt) contrast for imaging of brain tumors. *Magn Reson Med*, 50(6):1120–6, Dec 2003. 2

[8] Mohammad Haris, Anup Singh, Kejia Cai, Kavindra Nath, Rachelle Crescenzi, Feliks Kogan, Hari Hariharan, and Ravinder Reddy. Micest: a potential tool for non-invasive detection of molecular changes in alzheimer's disease. *J Neurosci Methods*, 212(1):87–93, Jan 2013. 2

[9] Kejia Cai, Anup Singh, David R Roalf, Ravi Prakash Reddy Nanga, Mohammad Haris, Hari Hariharan, Ruben Gur, and Ravinder Reddy. Mapping glutamate in subcortical brain structures using high-resolution glucest mri. *NMR Biomed*, Apr 2013. 2

[10] Feliks Kogan, Mohammad Haris, Anup Singh, Kejia Cai, Catherine Debrosse, Ravi Prakash Reddy Nanga, Hari Hariharan, and Ravinder Reddy. Method for high-resolution imaging of creatine in vivo using chemical exchange saturation transfer. *Magn Reson Med*, Feb 2013. 2

[11] Peter C M van Zijl and Nirbhay N Yadav. Chemical exchange saturation transfer (cest): what is in a name and what isn't? *Magn Reson Med*, 65(4):927–948, Apr 2011. 4, 19

[12] F. Bloch. Nuclear induction. *Phys. Rev.*, 70:460–474, Oct 1946. 5

[13] R V Mulkern and M L Williams. The general solution to the bloch equation with constant rf and relaxation terms: application to saturation and slice selection. *Med Phys*, 20(1):5–13, Jan-Feb 1993. 6, 13

[14] Donald E Woessner, Shanrong Zhang, Matthew E Merritt, and A Dean Sherry. Numerical solution of the bloch equations provides insights into the optimum design of paracest agents for mri. *Magn Reson Med*, 53(4):790–9, Apr 2005. 6, 8, 14, 15

[15] Kimberly L Desmond and Greg J Stanisz. Understanding quantitative pulsed cest in the presence of mt. *Magn Reson Med*, 67(4):979–90, Apr 2012. 8, 9, 15

[16] Zhongliang Zu, Ke Li, Vaibhav A Janve, Mark D Does, and Daniel F Gochberg. Optimizing pulsed-chemical exchange saturation transfer imaging sequences. *Magn Reson Med*, 66(4):1100–8, Oct 2011. 11

[17] Cynthia B Paschal and H Douglas Morris. K-space in the clinic. *J Magn Reson Imaging*, 19(2):145–159, Feb 2004. 11, 12

[18] N Gelman, J M Gorell, P B Barker, R M Savage, E M Spickler, J P Windham, and R A Knight. Mr imaging of human brain at 3.0 t: preliminary report on transverse relaxation rates and relation to estimated iron content. *Radiology*, 210(3):759–767, Mar 1999. 19

[19] Thomas Ethofer, Irina Mader, Uwe Seeger, Gunther Helms, Michael Erb, Wolfgang Grodd, Albert Ludolph, and Uwe Klose. Comparison of longitudinal metabolite relaxation times in different regions of the human brain at 1.5 and 3 tesla. *Magn Reson Med*, 50(6):1296–1301, Dec 2003. 19

[20] Greg J. Stanisz, Ewa E. Odrobina, Joseph Pun, Michael Escaravage, Simon J. Graham, Michael J. Bronskill, and R. Mark Henkelman. T1, t2 relaxation and magnetization transfer in tissue at 3t. *Magnetic Resonance in Medicine*, 54(3):507–512, 2005. 19

[21] Phillip Zhe Sun, Enfeng Wang, Jerry S Cheung, Xiaoan Zhang, Thomas Benner, and A Gregory Sorensen. Simulation and optimization of pulsed radio frequency irradiation scheme for chemical exchange saturation transfer (cest) mri-demonstration of ph-weighted pulsed-amide proton cest mri in an animal model of acute cerebral ischemia. *Magn Reson Med*, 66(4):1042–1048, Oct 2011. 19

[22] Dennis W J Klomp, Adrienne N Dula, Lori R Arlinghaus, Michel Italiaander, Richard D Dortch, Zhongliang Zu, Jason M Williams, Daniel F Gochberg, Peter R Luijten, John C Gore, Thomas E Yankeelov, and Seth A Smith. Amide proton transfer imaging of the human breast at 7t: development and reproducibility. *NMR Biomed*, Apr 2013. 23

[23] Craig K Jones, Daniel Polders, Jun Hua, He Zhu, Hans J Hoogduin, Jinyuan Zhou, Peter Luijten, and Peter C M van Zijl. In vivo three-dimensional whole-brain pulsed steady-state chemical exchange saturation transfer at 7 t. *Magn Reson Med*, 67(6):1579–1589, Jun 2012. 23

[24] Moritz Zaiss, Benjamin Schmitt, and Peter Bachert. Quantitative separation of cest effect from magnetization transfer and spillover effects by lorentzian-line-fit analysis of z-spectra. *J Magn Reson*, 211(2):149–55, Aug 2011. 24

[25] Jinyuan Zhou, He Zhu, Michael Lim, Lindsay Blair, Alfredo Quinones-Hinojosa, Steven A Messina, Charles G Eberhart, Martin G Pomper, John Laterra, Peter B Barker, Peter C M van Zijl, and Jaishri O Blakeley. Three-dimensional amide proton transfer mr imaging of gliomas: Initial experience and comparison with gadolinium enhancement. *J Magn Reson Imaging*, Feb 2013. 61